Supplementary Information

The potential for large-scale CO₂ removal via rock weathering on croplands

David J. Beerling[1]*, Euripides P. Kantzas[1], Mark R. Lomas[1], Peter Wade[1], Rafael M. Eufrasio[2], Phil Renforth[3], Binoy Sarkar[4], M. Grace Andrews[5], Rachael H. James[5], Christopher R. Pearce[6], Jean-Francois Mercure[7,8], Hector Pollitt[8,9], Philip B. Holden[10], Neil R. Edwards[8,10], Madhu Khanna[11], Lenny Koh[2], Shaun Quegan[12], Nick F. Pidgeon[13], Ivan A. Janssens[14], James Hansen[15] & Steven A. Banwart[16,17]

[1]Leverhulme Centre for Climate Change Mitigation, Department of Animal and Plant Sciences, University of Sheffield, Sheffield S10 2TN, UK

[2]Advanced Resource Efficiency Centre, Management School, University of Sheffield, Sheffield S10 1FL, UK

[3]School of Engineering and Physical Sciences, Heriot-Watt University, Edinburgh Campus, Edinburgh EH14 4AS, UK

[4]Lancaster Environment Centre, Lancaster University, Lancaster LA1 4YQ, UK

[5]School of Ocean and Earth Science, National Oceanography Centre Southampton, University of Southampton Waterfront Campus, Southampton SO14 3ZH, UK

[6]National Oceanography Centre, European Way, Southampton, SO14 3ZH, UK

[7]Global Systems Institute, Department of Geography, University of Exeter, Exeter, UK

[8]Cambridge Centre for Energy, Environment and Natural Resource Governance, University of Cambridge, Cambridge, CB3 9EP, UK

[9]Cambridge Econometrics Ltd, Covent Garden, Cambridge CB1 2HT, UK

[10]Environment, Earth and Ecosystems, The Open University, Milton Keynes, MK7 6AA, UK

[11]Department of Agricultural and Consumer Economics, Institute for Sustainability, Energy, and Environment, University of Illinois, Urbana, Illinois 61801, USA

[12]School of Mathematics and Statistics, Hicks Building, University of Sheffield, Sheffield S3 7RH

[13]Understanding Risk Research Group, School of Psychology, Cardiff University and the Leverhulme Centre for Climate Change Mitigation, Cardiff CF10 3AT, UK

[14]Research Group Plants and Ecosystems, University of Antwerp, Belgium

[15]Earth Institute, Columbia University, New York, NY, USA

[16]Global Food and Environment Institute, University of Leeds, Leeds LS2 9JT, UK

[17]School of Earth and Environment, University of Leeds, Leeds LS2 9JT, UK

*e-mail: d.j.beerling@sheffield.ac.uk

Supplementary Information

Contents

3. Tables   page

4. Supplementary references   53

1. Methods.

1.0 Conceptual model. The conceptual model underpinning our simulations is application of an annual load of crushed basalt of known particle size distribution and mineralogy to agricultural land. Carbon dioxide removal (CDR) results from the mass transport of enhanced weathering products liberated from the primary minerals, which are assumed to subsequently reach the surface ocean via continental runoff, or can be precipitated as secondary carbonate minerals in the terrestrial environment. The dissolution products result from the reaction of infiltrating water with the mass of basalt that is incorporated in the surface soil layer by spreading. The resulting dissolution products associated with CO_2 removal are the base cations (Ca^{2+}, Mg^{2+}, Na^+ and K^+) in soil drainage waters, and calcite precipitated within the soil profile. Simulations consider basalts exhibiting relatively slow-versus fast-dissolution rates due to differing mineralogy with different particle size distributions (Figs. S1-S2; Tables S1-S3). Basaltic minerals undergo dissolution at different rates, with some minerals continuing to undergo dissolution and capture CO_2 after the first year of application. Thus calculating representative annual CO_2 removal rates requires computing average rates derived from repeated basaltic rock dust applications. Therefore, we extended the theory underpinning our simulation framework by tracking cohorts of particles applied each year and their mineral composition over time to account for cumulative effects and report average CO_2 removal rates for 10-year simulations.

Mathematical representation of the conceptual model includes the reactive transport equation for solute advection with vertical 1-D transport model with steady-state flow (equations 1-6). Laboratory-determined rate laws for stoichiometric dissolution of each mineral define source terms for the liberated base cations in the 1-D transport equation (Tables S2, S3). Kinetic inhibition and affinity effects on mineral dissolution rates are included as a solubility limit for dissolved products of each primary mineral with pore fluids also in equilibrium with secondary minerals (calcite, amorphous silica, goethite, gibbsite). The conceptual model includes ion exchange equilibria between the pore fluids and a generic ion exchange surface with a cation exchange capacity representing agricultural soils (Table S4). The product of infiltration rate, land surface infiltration area over which the 1-D vertical transport applies, and the calculated dissolved concentrations at the base of the soil profile yield the enhanced weathering flux in drainage waters that contributes to CO_2 removal, along with calcium carbonate precipitation in the soil. We account for the mass depletion of dissolving minerals in the basalt and the effect of associated distribution of shrinking particle sizes and their resulting reactive surface areas. This model is represented by the following equations and coefficients.

1.1 Transport equation. The calculated state variable in the transport equation is the dissolved molar equivalents of elements released by stoichiometric dissolution of mineral i, in units of mole L^{-1}. ϕ is volumetric water content, C_i is dissolved concentration (mole L^{-1}) of mineral i transferred to solution, t is time (y), q is vertical water flux (m y^{-1}), z is distance along vertical flow path (m), R_i is the weathering rate of basalt mineral i (mole per litre of bulk soil per year) and C_{eq_i} is the solution concentration of weathering product at equilibrium with the mineral phase i[1,2].

$$\phi \frac{\partial C_i}{\partial t} = -q \frac{\partial C_i}{\partial z} + R_i \left(1 - \frac{C_i}{C_{eq_i}}\right) (1)$$

1.2 Mineral mass balance. The change in mass of basalt mineral i, B_i, is defined by the rate of stoichiometric mass transfer of mineral i elements to solution. Equation 2 is required because we are considering a finite mass of weathering rock, which over time can react to completion, as opposed to *in situ* weathering of the lithosphere, e.g. when considering weathering and geomorphology[2].

$$\frac{\partial B_i}{\partial t} = - R_i \left(1 - \frac{C_i}{C_{eq_i}} \right) \text{ (2)}$$

An additional transport equation for Ca ion (mol L^{-1}) is included for secondary mineral formation of the calcium carbonate phase calcite,

$$\frac{\partial Ca}{\partial t} = -q \frac{\partial Ca_{sol}}{\partial z} + \sum_{i=1}^{nmin} R(B_i) B_{ca_i} \text{ (3)}$$

where *nmin* is the number of minerals, $Ca_{sol} = \min(Ca, Ca_{sat})$ and C_{sat} is the concentration of Ca ion in pore fluids calculated to be in equilibrium with the carbonate mineral phase. We also define $Ca_{precip} = Ca - Ca_{sol}$. B_{ca_i} is the mass fraction of calcium within each mineral, Ca_{sol} is the concentration of calcium in solution and *Ca$_{precip}$* the calcium precipitate with units of concentration; all variables have units of mole/L.

Equations 1-3 form a coupled system of partial differential equations for all mineral components of the basalt and calcite, solved numerically with a Crank-Nicholson finite different scheme with discretised depth and time. Two additional equations are required to solve the system: a Dirichlet boundary condition at the soil surface $C = 0$ at $z = 0$, and a Neumann boundary condition at the bottom of the soil profile where the concentration gradient is set to zero. An initial condition is specified as a concentration field of zero mole L^{-1} at $t = 0$, and a specified initial basalt mass uniformly distributed vertically over the top 15 cm of soil.

We determined the values for C_{eq} for each of the mineral phases in the basalt grains by calibrating the results of the performance model against those of a 1-D reactive transport model (RTM) (Section 2.5). Calibration was undertaken against the time evolution of mass transfer for each mineral with minimisation of residual errors between the two sets of model results. The RTM incorporated the same kinetic reaction equations and full geochemical speciation equilibria for solutes and minerals including equilibria that describes cation exchange on soil exchange surfaces and the formation of secondary minerals. The RTM determines the ion activity product for dissolved species related to the solubility constant for each primary mineral and calculates from these a kinetic inhibition term that accounts for chemical affinity effects. Values for C_{eq} were calibrated for each basaltic mineral for a range of infiltration rates. We demonstrate with this approach that the simplified mass transfer inhibition term in equations 1-3 successfully described the same kinetic behaviour calculated by the RTM (Figs. S10-S12). For the basalts we considered, and under the soil conditions simulated, labradorite was the only mineral constituent that exhibited notable chemical inhibition.

1.3 The weathering source term. The mass transfer rate of each mineral phase to solution R_i depends on B_i and is a function of the weathering rate w_i for each mineral i normalised to reactive surface area, multiplied by the reactive surface area of each mineral SA_i which also changes as total mineral mass is depleted by dissolution. Parameter values for SA_i for each mineral in our model depend on geometric surface areas scaled by a roughness factor, which is modelled with a fractal dimension of 0.33 to account for the physical differences in laboratory and field weathering environments and differences between particle sizes[3] (Sections 1.6-1.7).

$$R_i = w_i(pH) \, SA_i \text{ (4)}$$

Soil pH of each grid cell is dynamically calculated from the alkalinity mass and flux balance for an adaptive time-step, controlled by mineral dissolution rates on mineral dissolution, following initialization with a topsoil (0-15 cm) pH value based on field data from global soil databases (Table S14); soil pH buffering capacity is accounted for with an empirical soil pH buffer function[4]. The soil pCO$_2$ depth profile of a grid cell is generated with the standard gas diffusion equation[5], scaled by crop NPP × 1.5 to account for combined autotrophic and heterotrophic respiration[6]. The alkalinity balance

considers net acidity input during crop growth for biomass-cations removed from the field[7], and secondary mineral precipitation of calcite, as described in Ref[8].

1.4 Removal of weathering products. The total mass balance over time for basalt mineral weathering allows calculation of the products transported from the soil profile.

$$\int_0^L B(t,z)\,\mathrm{d}z = \int_0^L B(0,z)\,\mathrm{d}z - \phi \int_0^L C(t,z)\,\mathrm{d}z - q \int_0^t C(t,L)\,\mathrm{d}t \ (5)$$

The total mass of weathering basalt is defined as follows, where m is the total number of weathering minerals in the rock, t_f is the duration of weathering (year) and L is the total depth of the soil profile.

$$\text{Total weathered Basalt} = \sum_{i=1}^{m} \phi \int_{z=0}^L C_i(t,z)\,\mathrm{d}z + q \int_{t=0}^{t_f} C_i(t,L)\,\mathrm{d}t \ (6)$$

We define q as the net annual sum of water gained through precipitation[9] and irrigation[10], minus crop evapotranspiration[11], as calculated with high spatial resolution gridded datasets (Table S14).

1.5 Rate law. We modelled application of a crushed fast- or slow-weathering continental flood basalt, with specified mineral weight fractions and physical characteristics (Tables S1-S3). Rates of basalt grain weathering define the source term for weathering products and are calculated as a function of soil pH, soil temperature, soil hydrology and crop net primary productivity (NPP). The inorganic general rate law for each mineral, using the linear transition state theory rate law[12,13], is given as:

$$\mathrm{w} = \sum_i k_i \exp\left[\frac{-E_i}{R}\left(\frac{1}{T} - \frac{1}{298.15}\right)\right] a_j^{n_i} \ (7)$$

where i is the individual weathering agent, e.g. [H$^+$], [H$_2$O], [OH$^-$], k_i is the rate constant (mol m^{-2} s^{-1}), E_i is the apparent activation energy (kJ mol^{-1}), R is the gas constant (kJ mol^{-1} K^{-1}), T is temperature (K), a_j is the molar activity of weathering agent j (mol l^{-1}), n_i is the reaction order. To account for chemical affinity effects, the term w is multiplied by a chemical affinity term $(1-C/C_{eq})$ in the reactive transport equation (equations 1-2). Parameters k_i, E_i and n_i for all basaltic minerals modelled are listed in Table S3. This version of the model (equation 7) is well-validated against flask-dissolution experiments (Fig. S3).

In equation (7), T equals soil surface temperature of a grid cell, defined as the mean value at 5 cm depth of the 8 warmest months for 2050 (Table S14). This value is taken to represent conditions during the main growth period of most crop types found outside the tropics. In the tropics and sub-tropics, where perennial crops dominate, annual temperature variation is relatively low.

1.6 Reactive mineral surface area. The reaction rate of a mineral undergoing dissolution in soil is governed by the law of kinetic mass action and is proportional to the moles of reactive sites on the mineral surface in contact with the reacting aqueous solution[14]. The general kinetic rate law includes the term for total reacting surface area (SA_i, m^2) (equation 6) and the reactivity of the specific mineral surface is reflected in the kinetic rate constant (k_i, mol m^{-2} s^{-1}) (equation 7). The reactive surface area of the mineral usually scales by amount of mineral. Thus a useful parameter to use when calculating the surface area of a mineral is the specific surface area (SSA), which is the reactive surface area (SA_i) normalised to mass of mineral i (m_i).

1.7 Surface roughness. The measured SSA of a granular material is typically much higher than estimates of the surface area by geometric models of particle shapes, due to surface topography and porosity effects[15]. Discrepancies between measured surface area and that calculated from particle geometry are accounted for using a surface area multiplier, defined as the surface roughness factor, λ, which accounts for topography and porosity effects.

We adopt a methodology that treats basalt reactive surface as a fractal[3]. The fractal dimension provides a means of consolidating measurements taken at different scales. At the particle scale we

model the surface area geometrically and relate it to the radius of individual particles. Using this methodology, the resultant scaling for the roughness factor is given by equation 8.

$$\lambda = \left(\frac{\beta}{a}\right)^d \quad (8)$$

where a is the spatial constant related to the scale of measurement of BET surface area (10^{-10}m), β is the scale at which the rates are being determined (particle radius) and d is the fractal dimension. The fractal dimension and its uncertainty are determined from a linear regression analysis performed on measurements from a range of spatial scales[3] (10^{-10}-10^3m).

The weathering rate of the mineral i is proportional to the product of the surface roughness, the specific surface area *in situ* (SSA_i) and the mass of the mineral (m_i).

$$R_i = w_i \, \lambda \, SSA_i \, m_i \quad (9)$$

1.8 Particle size distribution weathering. Standard calculations of rate of mineral dissolution ignore size differences in reacting particles and simulate the mineral with a surface area that corresponds to the mean diameter of a particle size distribution (psd). However, mechanical comminution produces an approximately log-normal psd[16] that varies with different grinding and milling technologies. We therefore use two different log-normal psd[17,18] which arise from two different grinding technologies and average the simulation results from using the different distributions.

We use a shrinking grain model to simulate a continuous range of weathering particle sizes. To introduce the level of "grinding" into the model, we assume that grinding scales the particle diameter so that the normalised mass distribution is given by a shape and a scale value. The scale value used here is a "*px*" value, which is defined to be the diameter for which x% of the mass is made up from particles with smaller diameters: *p80* values are often used as a scalar description of a distribution.

We derive the unique SA-mass relationship for a given psd to calculate weathering in equation (4) as follows. A psd can be fully described by a mass density function. We denote this as the initial condition to the general time-varying psd, $f(t,r)$, where r is particle radius for $t = 0$, such that the mass of particles having radius greater than r_1 and less than r_2 at time t is given by:

$$M(t) = \int_{r_1}^{r_2} f(t,r) \, dr \quad (10)$$

and the total mass of the particles at time t is given by:

$$M(t) = \int_0^\infty f(t,r) \, dr \quad (11).$$

The surface area of particles of radius, r, and mass, m, is given by:

$$SA = \frac{3\,m}{\rho\,r} \quad (12)$$

and the surface area of particles described by a psd is given by:

$$SA(t) = \frac{3}{\rho} \int_0^\infty \frac{f(t,r)}{r} \, dr \quad (13).$$

The weathering model generally has the form:

$$\frac{dM}{dt} = -w \, \lambda \, SA \quad (14).$$

where SA is the geometric surface area, λ is roughness and w is the weathering rate (determined by kinetic parameters, soil temperature and pH and NPP). As particles are assumed to be spherical, we reformulate equation 14 in terms radius rather than mass to give:

$$\frac{dr}{dt} = -\frac{w\,\lambda(r)}{\rho} \quad (15)$$

Given our fractal assumption of roughness:

$$\lambda(r) = \gamma r^d \quad (16)$$

where $\gamma = (10^{10})^d$. Equations 15 and 16 can be combined and solved analytically, and given the initial condition $r = r_0$ at $t = 0$, then.

$$r(t) = \left(r(0)^{1-d} - [1-d]\frac{\omega\gamma}{\rho}t\right)^{\frac{1}{1-d}} \quad (17)$$

The reactive surface area, accounting for roughness is given by:

$$SA(t) = \frac{3}{\rho}\int_0^\infty \frac{\lambda(r)\,f(t,r)}{r(t)}dr \quad (18).$$

Using the above framework, we derive a pair of parametric equations for SA and describe mass in terms of time: $R(B)$. To do this we consider an infinitesimal range of particles within the psd $r(0) < r < r(0) + \delta r(0)$ having mass density $f(0, r(0))$. After weathering for a time t, $r(0)$ is mapped to $r(t)_*$ with corresponding mass density $f(t, r(t))$ and range $\delta r(t)$.

The mass density of the weathered particle can be determined by mass balance. The ratio of the mass of the weathered and un-weathered particles is equal to the cube of the ratio of the respective radii, giving.

$$\frac{m(t)}{m(0)} = \frac{f(t,r(t))\,\delta r(t)}{f(0,r(0))\,\delta r(0)} = \left(\frac{r(t)}{r(0)}\right)^3 \quad (19)$$

In the limit, and using equation (15), we can obtain the following expression for the weathered mass density function in terms of the initial PSD and time.

$$f(t,r(t)) = f(0,r(0))\left(\frac{r(t)}{r(0)}\right)^3 \frac{dr(0)}{dr(t)} = f(0,r(0))\left(\frac{r(t)}{r(0)}\right)^3 \frac{dr(0)}{dt}\Bigg/\frac{dr(t)}{dt}$$

$$= f(0,r(0))\left(\frac{r(t)}{r(0)}\right)^3 \frac{\lambda(r(0))}{\lambda(r(t))} \quad (20)$$

Substituting into equation 13 gives an expression for the geometric surface area:

$$SA(t) = \frac{3}{\rho}\int_0^\infty f(0,r(0))\left(\frac{r(t)}{r(0)}\right)^3 \frac{\lambda(r(0))}{\lambda(r(t))}dr \quad (21)$$

Whilst the reactive surface area, equation 18, is given by the first parametric equation:

$$SA(t) = \frac{3}{\rho}\int_0^\infty f(0,r(0))\left(\frac{r(t)}{r(0)}\right)^3 \lambda(r(0))\,dr \quad (22)$$

The mass corresponding to the psd is given by the second parametric equation:

$$M(t) = \frac{4\pi\rho}{3}\int_0^\infty r(t)^3\,dr \quad (23)$$

1.9 Multi-year basalt applications. To model repeated basalt applications, the psd of the existing basalt (f_1) is combined with the psd of the new application (f_2). As the existing psds at each soil level are at different stages of weathering, calculating the combined psd requires the psds at each level and each mineral to be calculated. Given the existing mineral mass, these can be calculated prior to the application using the equation (20). The new psd is given by the sum of the existing (f_1) and application (f_2) psds, such that the basalt mass distribution after application is given by equation (24), as shown by psd definition (equation 10).

$$M(t) = \int_{r_1}^{r_2} f_1(t,r) + f_2(t,r)\, dr \ (24)$$

2.0 Plant-assisted weathering. Plant-enhanced basalt weathering is modelled empirically for annual and woody crops with power functions fitted to data (Fig. S4; Table S5). These functions represent the effects of a range of rhizosphere processes that accelerate the physical breakdown and chemical dissolution of minerals, including the activities of nutrient scavenging mycorrhizal fungi that physically disrupt and chemically etch mineral surfaces, and bio-production of low molecular weight organic compounds and chelating agents[19,20]. The power functions relate normalised NPP (NPP_{norm}), and the NPP multiplier of the rate equation, $f(NPP_{a,w})$, for annual and woody crops as follows:

$$f(NPP_{a,w}) = NPP_{enhancement} = a(x_{norm} NPP_{norm})^b + 1 \ (24)$$

where a, x_{norm} and b are fitted parameters for annual and woody crops (Table S5).

Incorporating the plant weathering functions yields:

$$Rate_m = SA_m \sum_i [k_{i,m} \exp[\frac{-E_{i,m}}{R}(\frac{1}{T} - \frac{1}{298.15})] a_i^{n_{i,m}}] f(NPP_{a,w}) \ (25)$$

We used gridded data for 175 crops (yield and harvested area)[21,22] (Table S14) with yield converted to NPP using standard procedures[22] and linearly scaled to a 0-1 range and NPP values capped at the 99% percentile.

2.1 Carbon dioxide removal. We calculate carbon dioxide removal (CDR) by ERW of crushed basalt applied to soils via two pathways: 1) the transfer of weathered base cations (Ca^{2+}, Mg^{2+}, Na^+ and K^+) from soil drainage waters to surface waters that are charge balanced by the formation of HCO_3^- ions, which are transported to the ocean and 2) formation of pedogenic carbonates. A generalised version of calcium silicate mineral dissolution representative of Pathway 1 is given by equation 26. If some of the resulting HCO_3^- is precipitated as calcium carbonate, CDR follows Pathway 2 (equation 27).

Pathway 1 for calcium ions:

$$CaSiO_3 + 2CO_2 + 3H_2O \rightarrow Ca^{2+} + 2HCO_3^- + H4SiO_4 \ (26)$$

Pathway 2 for calcium carbonate formation:

$$Ca^{2+} + 2HCO_3^- \rightarrow CaCO_3 + CO_2 + H_2O \ (27)$$

Monovalent and divalent base cations are released from basaltic minerals by dissolution based on stoichiometry (Table S2). CDR, via pathway 1, potentially sequesters two moles of CO_2 from the atmosphere per mole of divalent cation. However, ocean carbonate chemistry reduces the efficiency of CO_2 removal (η) to an extent depending on ocean temperature, salinity and the surface ocean dissolved CO_2 concentration. We calculate η for average ocean temperature (17 °C), salinity (35%) and an RCP8.5 2050 dissolved pCO_2 of 600 µatm, giving η = 0.86, i.e., 0.86 mole of CO_2 removal per mole of monovalent cation and 1.72 mol of CO_2 removed per mol of divalent cation added to the oceans[23]. For Pathway 1, the efficiency of CDR $= \eta \times \sum$(mol monovalent cations)$+2\eta \times \sum$(mol divalent cations).

CDR via pathway 2 occurs if dissolved inorganic CO_2 precipitates as pedogenic carbonate, and sequesters 1 mol of CO_2 per mole of Ca^{2+} instead of 1.72 mol of CO_2 via pathway 1 and is therefore less efficient. Thus for any given grid cell, we compute CO_2 removal by ERW as the alkalinity flux in soil drainage and pedogenic calcite precipitation. Possible CO_2 degassing due to changes in surface water chemistry during transport in large river systems[24] is not considered. We assume land management practices for annual crops return cations released during dissolution, and taken up by crops back to soils via biomass decomposition. This is in addition to elements removed in harvest, which are returned via element cycling through the animal and human food chains. This assumption reflects practices of removing primarily grain biomass from fields and returning the shredded fast-decomposing organic residues back to soil. For perennials, e.g., palm oil plantations, cations accumulated in living biomass is accounted for by the stoichiometry of NPP.

2.2 Cost assessment modelling. A breakdown of mining costs was obtained using a three-step engineer-based itemized approach[25]. Step 1 involves determining the design of a mine to the maximum extent possible, step 2 considers the labour, equipment fleet and consumables required to establish and operate the mine, and step 3 involves the use of specialized, commercially available databases[26] holding unit costs for labour, equipment and consumables.

We adopt a prior detailed analysis based on this methodology with reference to an open pit mine located in USA, which extracts 10,000 tonnes of ore per day at a 1:1 strip ratio, typical for basalt mines[25]. The cost breakdown allows us to convert these costs to country-specific values using diesel prices and gross national income as normalization factors. To achieve this we assign to each component cost $C(i)$ three weights that sum up to 1; w_f is the fraction of the particular cost due to fuel, w_l due to labour and w_s the fraction of the cost independent of fuel and labour, signifying here the cost of specialized equipment. Each component cost for a particular country k now becomes:

$$C(i)_{[k]} = C(i)_{[USA]} \left(w_f \frac{Diesel_{[k]}}{Diesel_{USA}} + w_l \frac{Income_{[k]}}{Income_{USA}} + w_s \right) (28)$$

where $Diesel_{[k]}$ and $Income_{[k]}$ are the diesel price and gross national income, respectively. The component costs and relevant weights, the latter of which are based on assumptions regarding the nature of each cost, are given in Supplementary Information. For the USA, mining cost is 6.99 \$ t^{-1} as obtained from prior analysis[22]. Mining costs for China, India, Indonesia, Mexico, Canada and Brazil calculated using the method were 5.33, 4.44, 3.97, 4.88, 6.79 and 5.42 \$ t^{-1}, respectively and for France, Germany, Poland, Italy and Spain 7.90, 8.26, 6.76, 8.30 and 7.31 \$ t^{-1}, respectively. The lower price for China, India and Brazil reflects low labour costs while the higher price for France and Germany reflects higher diesel costs.

Distribution costs and emissions were calculated by performing spatial analysis with ArcGIS software. Basalt rock sources were identified from the GLiM rock database[27], excluding those in protected areas[28]. We then performed a global transport (rail and road) network analysis by modelling a logistic ERW supply by creating an Origin-Destination Cost Matrix using GIS[29,30]. For larger datasets, the Origin-Destination cost matrix searches and measures the least-cost paths along the network from multiple origins to multiple destinations to identify the most cost-effective or shortest route between a source and destination.

Transport analyses used the lowest emission option between rail and road network to calculate distribution costs and CO_2 emissions (summarized in Tables S10-S12). Freight-rail emissions were obtained from 2050 projections of reduced carbon emissions following improvements in energy efficiency[31]. Rail CO_2 emissions were thus the same for both the business-as-usual (BAU) and 2°C scenarios. For road transport, we considered estimated energy consumption of currently/shortly available heavy electric trucks 1.38 (kWh/km)[32] and projected carbon emissions in the electricity

sector of each country for BAU or the 2°C scenario[33]. Finally, the cost of both transport systems is based on current diesel (litres per km) and electricity prices (Kwh per km) in each country[34].

Cost of spreading rock with farming machinery was considered equivalent to that of spreading lime ($15.18/t). We assigned 50% of the spreading costs to fuel consumption and 50% to labour, investment and other costs. Spreading costs, $C_{S[k]}$, in $/t for a country k were then calculated as the weighted sum of diesel fuel prices and labour costs, both normalized to UK values

$$C_{S[k]} = \left(0.5\frac{Diesel_{[k]}}{Diesel_{UK}} + 0.5\frac{Income_{[k]}}{Income_{UK}}\right)15.18 \text{ (29)}$$

Total costs were calculated for each country k as

$$C_{Tot[k]} = (C_{M[k]} + C_{T[k]} + C_{S[k]})App_{Rock[k]} \text{ (30)}$$

where App_{Rock} is the total rock applied. Our cost are indicative of key features of an ERW supply chain and consistent with previous global approaches. Variation in these costs are expected and supply chains may be designed to optimise regional or national price variability. No account is taken of wider impact of ERW supply chains on other markets.

2.3 Optimization. We formulated the relationship between particle size diameter (µm) and surface area (m²/g), as well as surface area (m²/g) and grinding energy per unit mass (MJ/t) using prior results[35] combined to derive an expression for the relationship between particle size $p80$ (µm) and the grinding energy G_{EN} required to grind a unit mass (MJ/t).

$$G_{EN}(p80) = a_3[e^{a_4 log_{10}(a_1 p80 + a_2)}] \text{ (31)}$$

with a_1=-4.46, a_2 = 11.57, a_3 = 49.47 and a_4 = 0.26.

We used country-specific electricity production (P_{Grid}) and the forecast fractional contributions to electricity production by different energy sources (coal, natural gas, oil, solar PV, concentrated solar power, hydropower, wind, marine) for 2050 based on business-as-usual (BAU) energy polices and energy projections consistent with a 2°C (2°C) warming scenario[33]. National CO_2 emissions (C_EG) for electricity generation consistent with both scenarios were based on results reported in Ref[33] (Tables S6-S9). Industrialized nations (e.g., Canada) consume up to ~2% of their total energy production on rock comminution (crushing and grinding) processes[36]. We assume a future limit of 3% for all nations, based on the rationale that current rates for developed nations grow from around 2% today in-line with future energy scenarios[33].

For a grid cell i where rock is applied, the net emissions E_{NET} (mass CO_2) for a particle size distribution defined by $p80$, are given by

$$E_{NET}(p80|i) = E_G(p80|i) + E_w(p80|i) \text{ (32)}$$

where E_G is grinding emissions and E_W is gross CO_2 sequestration, considered here as a negative flux.

Grinding and weathering CO_2 emissions were calculated as:

$$E_G(p80|i) = App_{Rate}App_{Area}(i)C\_EG(i)G_{EN}(p80) \text{ (33)}$$

$$E_w(p80|i) = -Q_{CO2}(p80|pH(i), temp(i), NPP(i))App_{Rate}App_{Area}(i) \text{ (34)}$$

where App_{Rate} is the rock application rate (mass rock/area), App_{Area} is the cropland area of the grid cell where the rock is applied (Area), C_EG is emissions of the electricity grid for the grid cell (Mass CO_2/Energy) and G_{EN} the energy required to grind a unit mass of rock at a particular $p80$ (Energy/Mass Rock) obtained from equation 30. Q_{CO2} is the mass ratio of CO_2 sequestered to rock applied (unitless) calculated as a function of $p80$ and grid cell pH, temperature (temp) and scaled NPP.

For a country comprised of k grid cells we minimize the k-element vector $\overrightarrow{p80}$

$$I(\overrightarrow{p80}) = \Sigma_i^{[k]} E_{NET}(p80_i|i) \quad (35)$$

with the additional non-linear constraint that the grinding energy cannot exceed a certain fraction a, in this case 0.03, of the country's projected grid electricity production P_{Grid} (Energy) for the year 2030

$$\Sigma_i^{[k]} App_{Rate} App_{Area}(i)(p80(i)) \leq aP_{Grid} \quad (36)$$

Secondary emissions from mining (M), transporting (T) and spreading (S) rock were not considered during optimization, as they are independent of particle size. They are taken into account as:

$$\Sigma_i^{[M,T,S]} Q_{CO2}(i) App_{Rate} App_{Area} \quad (37)$$

Q_{CO2} values for transporting and spreading rock were obtained from our GIS analyses (Supplementary Information). For the optimization, we used MATLAB's pattern search algorithm[37].

The high-resolution driving data sets means there are on the order of 10,000-100,000 k grid cells for each country's crop area, making a constrained, non-linear optimization unfeasible in terms of computational resources. To overcome this, and prior to optimization, we perform a k-means clustering (classification) for each country's k grid cells creating 60-75 classes; each one has a temperature, pH and NPP enhancement factor assigned as the centroid of each cluster and an area as the sum of areas of the grid cells that belong to the specific class. We use these 60-75 classes for optimization and the resulting $p80$ for each class is then assigned to all the grid cells in it. Although the number of grid cells to be optimized is reduced by orders of magnitude during the classification, the approximation proved robust with small error and bias when tested at low resolution due to small intra-class variability.

The above process calculates the optimized $p80$ grid cell vector and was conducted for different fractions of a country's crop area (0.1 to 1.0 at 0.1 increments), ordered according to weathering potential. For a given $p80$ value, we calculate the weathering rate for each grid cell, sort them in descending order and find the grid cells that comprise the cumulative area fraction for each increment. Optimization is conducted for each combinations of the two types of basalt and the two quasi-log-normal particle size distributions for each country. Uncertainty in the fractal dimension affects weathering rate and consequently, through the optimization, the $p80$ grid cell vector. We used Monte Carlo sampling ($n \approx 100$) to approximate the resulting distribution of $p80$ for each grid cell. Results are shown for the median $p80$ value for each grid cell when the Monte Carlo distributions for the combinations of basalts and particle size distributions are pooled.

2.4 Forecasting bulk silicate waste production. A model that relates global per capita material production (for cement) or consumption (steel) P to per capita gross world product (GWP)[38,39] was regressed through historical global data using nonlinear least squares (equation 38).

$$P = ae^{-b/GWP} \quad (38)$$

where a and b are regression constants. The derived saturation value, a, was used in a further regression through national data normalised to 2014 production and GDP (equation 39).

$$P = P_{REF} \times (1 + ((m+r) \times \Delta GDP) \times e^{(a \times (1-e^{-(m \times \Delta GDP)})) - (m \times \Delta GDP)} \quad (39)$$

where P_{REF} is the global per capita consumption in a given reference year (2014) and ΔGDP is the deviation of the per capita gross domestic product from the reference year. Here, m and r are regression constants. These were used together with averaged projections of future GDP (Table S14) from the 'middle-of-the-road' Shared Socioeconomic Pathway (SSP2) to derive nationally resolved projections of future per capita consumption/production[40]. SSP2 potentially represents the largest

material production pathway, as other SSPs forecast lower consumption or economic growth producing 30-50% less material globally. We have not considered the penetration of recycling into steel production beyond its current rate. Cement and cement kiln dust have no capacity to be recycled as cement. The total production/consumption at a given time, $T(t)$, was calculated by multiplying the population, $Pop(t)$, by production or consumption (P) (equation 40):

$$T(t) = P(\Delta GDP) \times Pop(t) \quad (40)$$

We assume 115 kg of cement kiln dust is produced as a by-product in kilns for every tonne of clinker, and have modelled the production of demolition waste following an average 50-year service life (normally distributed with a standard deviation of 10 years)[41]. The ratio of pig iron to steel production (0.72) was obtained using linear regression of 1960-2014 data, negating the need to explicitly model pig iron displacement from scrap recycling, and assuming the scrap ratio remains unchanged. All steel and blast furnace slag was considered available for reaction with CO_2. Between 2006–2014, 185 kg of blast furnace slag and 117 kg of steel slag was produced for every tonne of crude steel[42].

2.5 1-D reactive transport modelling(RTM)

We constructed a 1D-RTM to assess the effect of the chemical affinity term on mineral weathering from basalt rock particles in soil with the PHREEQC modelling code and a widely adopted thermodynamic database[43]. The structure of the porous medium for flow and transport is specified with a flow porosity of 25%[44]. The RTM simulates the top 150 mm layer of the soil column, i.e., the depth to which powdered basalt is added in the simulations (application rate of 40 t ha^{-1}), and calculated on a numerical grid of 15 × 10 mm thick cells, with a defined constant water flux. Basaltic minerals are distributed evenly over the simulated depth and weather according to their respective kinetic mass action laws for the mineral dissolution reactions (Tables S1-S3). Chemical affinity effects were accounted for with a chemical inhibition term which slows the dissolution rate as the chemical state of the fluid approached equilibrium with the respective mineral phases. Interstitial waters are calculated to be in equilibrium with the dissolved weathering products, inorganic and organic soil cation exchange surfaces and secondary minerals. These were calculated to form and dissolve instantaneously to maintain thermodynamic equilibrium between the fluid and mineral phases.

Initial exchangeable concentrations on the inorganic exchange surfaces were determined by equilibrating a characteristic soil pore water chemistry with a representative cation exchange capacity (Table S4) The soil solution was equilibrated with dissolved O_2 and CO_2; assuming equilibrium with atmospheric pO_2(g) (atm). Soil CO_2 gas phase concentration varied with depth with the diffusion equations[5,6] as for the performance model.

The mass and surface area of reacting minerals were based on their relative concentration in the initially applied basalt, and modelled using a shrinking core model. Reactive surface area was based on a uniform particle size characteristic of rock flour[17] with a diameter of 12 μm, a basalt density of 3.0 g/cm^3 and accounting for the fractal dependence of surface properties on the physical scale of the weathering system (see Sections 1.6-1.7). These basalt characteristics are shared with our performance model. Potential secondary mineral phases consistent with early stages of basalt weathering[45] were determined to be those exhibiting oversaturation with respect to the evolving pore water chemistry and that are known to react reversibly on the relatively short residence times of the soil fluids[14]. From this rationale, we included secondary mineral formation of calcite, amorphous silica, gibbsite and goethite. Formation of these secondary minerals respectively creates sinks for dissolved calcium, silicon, aluminium and iron. An additional sink for cations released by basalt weathering considered in the RTM simulations was cation exchange on soil clay minerals.

Results of sensitivity analysis undertaken for three infiltration rates (200 mm yr^{-1}, 600 mm yr^{-1} and 1,200 mm yr^{-1}) with and without the chemical affinity term at 25 °C are presented in Fig. S6 with corresponding secondary mineral precipitates in Fig. S7. The baseline analysis considered the possible precipitation of calcite, gibbsite, amorphous silica (SiO_2) and goethite over a range of infiltration rates of 200-1200 mm/y (desert to wet tropics). This baseline comparison is compared with simulations in which we considered 1) the formation of cation-retaining smectite in addition to the gibbsite, calcite, goethite and SiO_2, and 2) kaolinite as the most stable clay mineral end-product of weathering over longer time periods[8]. Allowing formation of either secondary clay mineral accelerated dissolution of basaltic minerals through suppression of Al ion activity in solution resulting in less kinetic inhibition of the dissolution reactions (Fig. S8, S9). These results suggest that our approach, which does not explicitly account for the effects of secondary clay minerals on acceleration of primary mineral dissolution, is conservative with respect to calculating basalt dissolution.

We show close correspondence between the results of the RTM with full chemical speciation and our simplified performance model for the weathering of either type of basalt (tholeiitic and alkaline) being considered (Figs S10, S11). Agreement between modelling approaches holds across a wide range of flows. Weathering inhibition appears negligible over the 1 year duration of soil weathering, other than for laboradorite, with the performance model realistically capturing the effects of chemical affinity. In summary, our calibrated performance model explicitly calculates pedogenic calcium carbonate formation and implicitly accounts for the effects of amorphous silica, goethite and gibbsite formation. As a result, the two approaches (RTM and performance model), give similar patterns of alkalinity release, pedogenic carbonate formation and CO_2 removal (Fig. S12) to underpin our modelling approach.

(a)   (b)

Mass Distribution   **Mass Distribution**
Renforth   **Cepuritis_1-25**
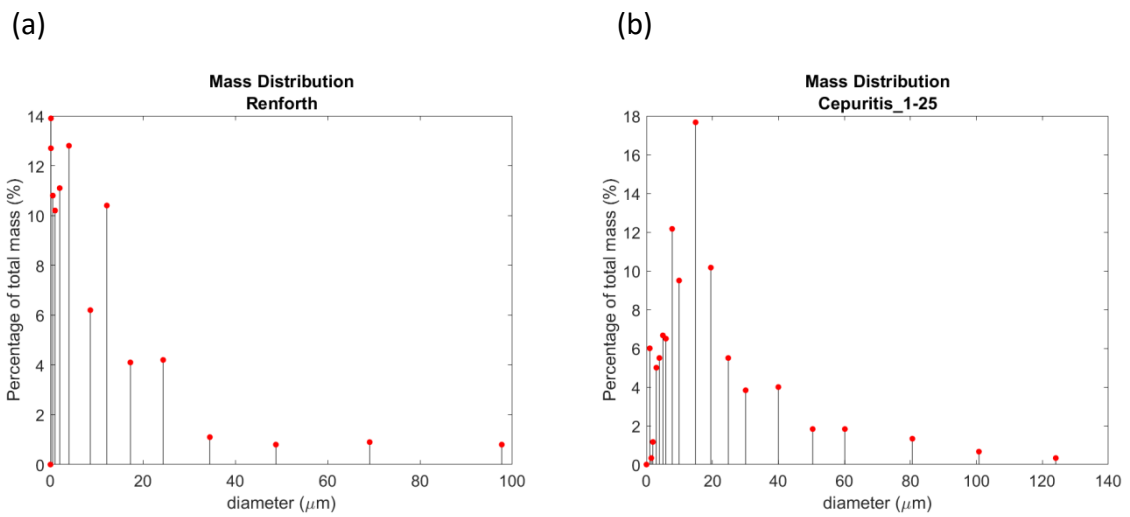
Figure S1. *Mass distribution profiles of ground rock*. Percentage of samples by mass of particles of ground basaltic rock as a function of diameter in (**a**) Renforth[17] and (**b**) Cepurtis *et al.*[18].

(a)

(b)

(c)

(d)
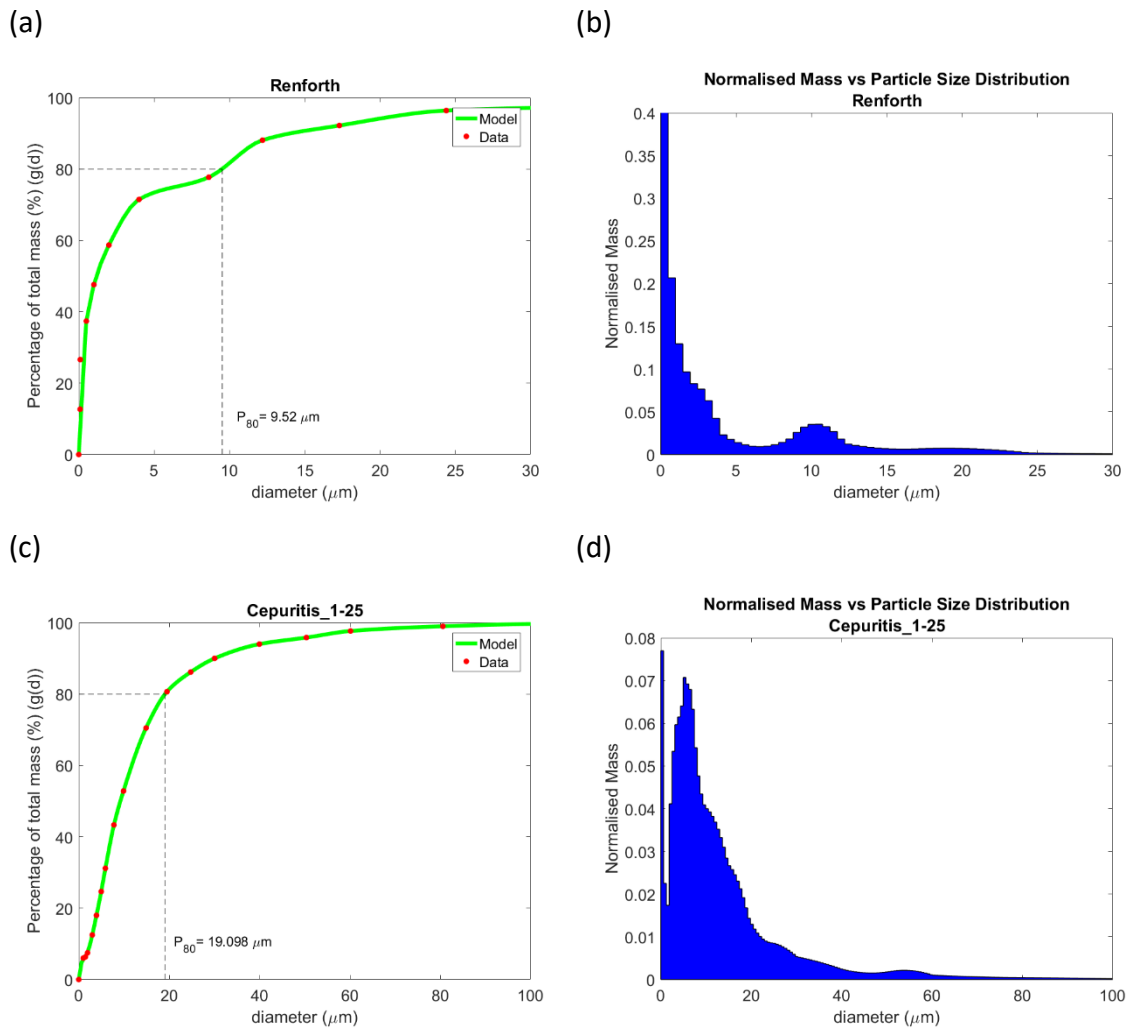
Figure S2. *Particle size distributions of ground rock profiles.* (**a**) Plot of percentage of mass contained in ground basalt particles below a given diameter (Renforth profile)[17], (**b**) The associated normalised mass distribution function of particle diameter. (**c**) and (**d**) are corresponding plots derived from the Cepurtis[18] profile.

(a)
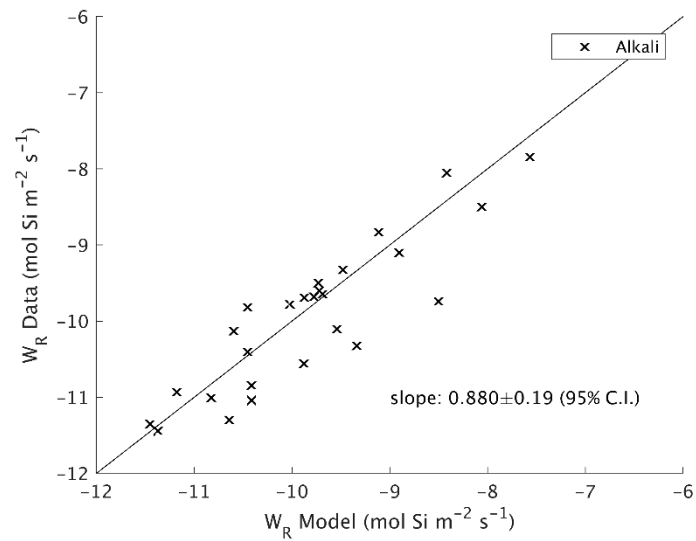
(b)
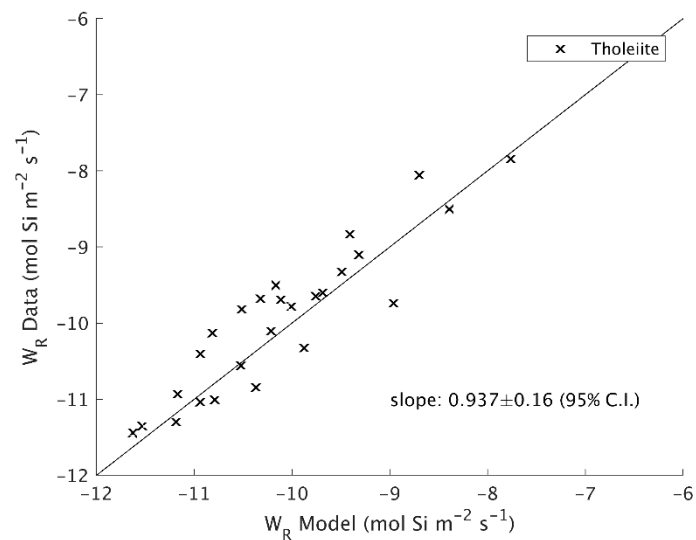
Figure S3. *Model validation.* Plots show predicted weathering rate (W_R, $\log_{10}$ scale) with our performance model rate equation (Si-release) validated against observations of flask-based weathering rates, based on an extensive data compilation[14], for (**a**) the alkali basalt (fast weathering) and (**b**) tholeiitic basalt (slow weathering). Weathering rates between the two types of basalt differ by a factor of 2; about 0.3 on the $\log_{10}$ scale of the plots. Slopes are not significantly different from 1 (*F*-test, *P* < 0.001 for both plots).

(a)
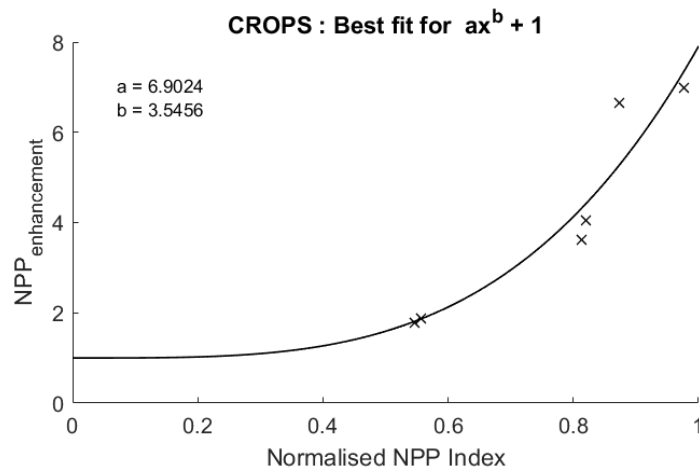
(b)
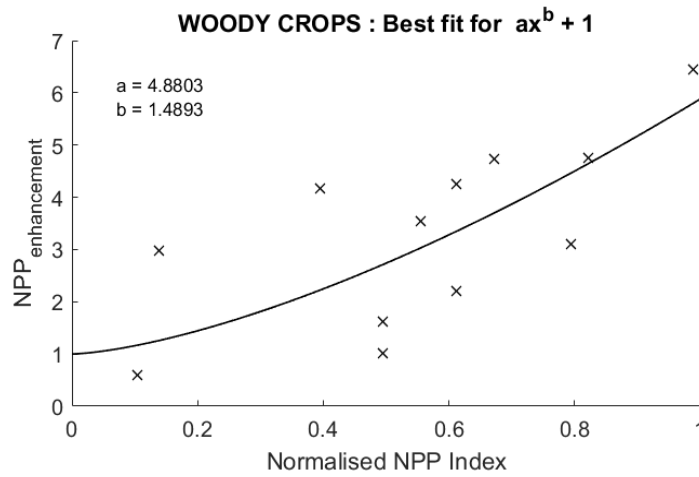
Figure S4. *Normalized functions for biotic weathering enhancment (NPP$_{enhancement}$) by crops.* Functions are fitted to mesocosm data for (**a**) three speies of agricultural crops (maize, rice and soybean)[46,47], and (**b**) four species of mycorrhizal tree saplings[48,49]. Table S5 gives parameter values for (**a**) and (**b**). These functions represent the lumped effects of rhizosphere biological processes accelerating weathering (Section 1.9).

(a)
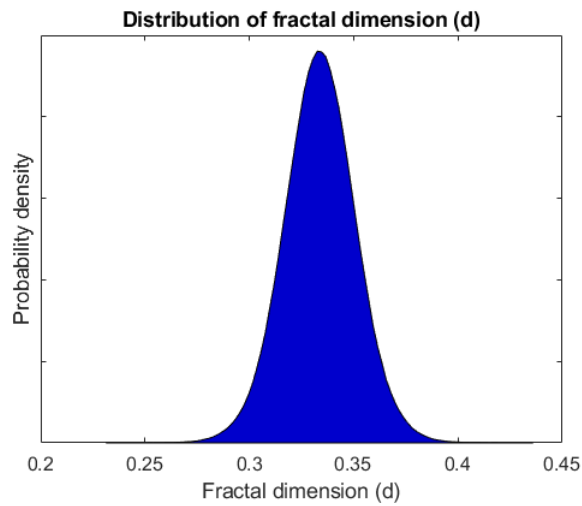
(b)
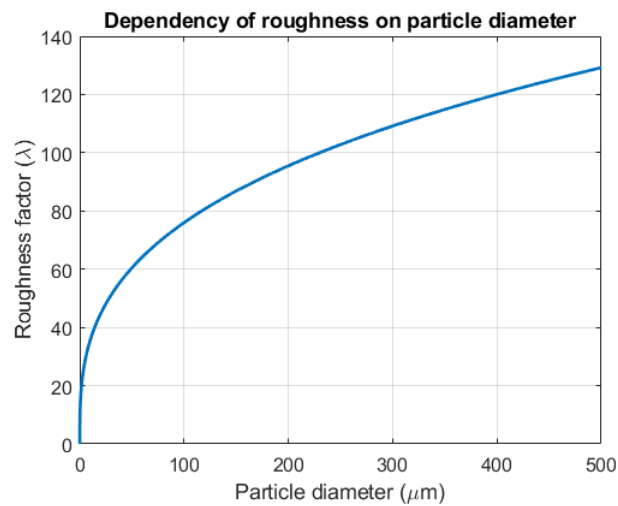
Figure S5. *Fractal dimension uncertainty and roughness factor scaling.* (**a**) Probability density function (PDF) of the fractal dimension (*d*) and (**b**) calculated relationship between roughness factor (lambda) and particle diameter. For comparison, basaltic glass powder with a diameter of 40 - 120μm has a lambda[50] of ~92. The PDF for the slope of the regression was calculated[51] using standard regression analysis for the slope (β) of the regression (using the data from Ref[3]): $\beta \sim 0.0163\ t_{20} + 0.33$, where t_{20} denotes a *t*-distribution with 20 degrees of freedom.
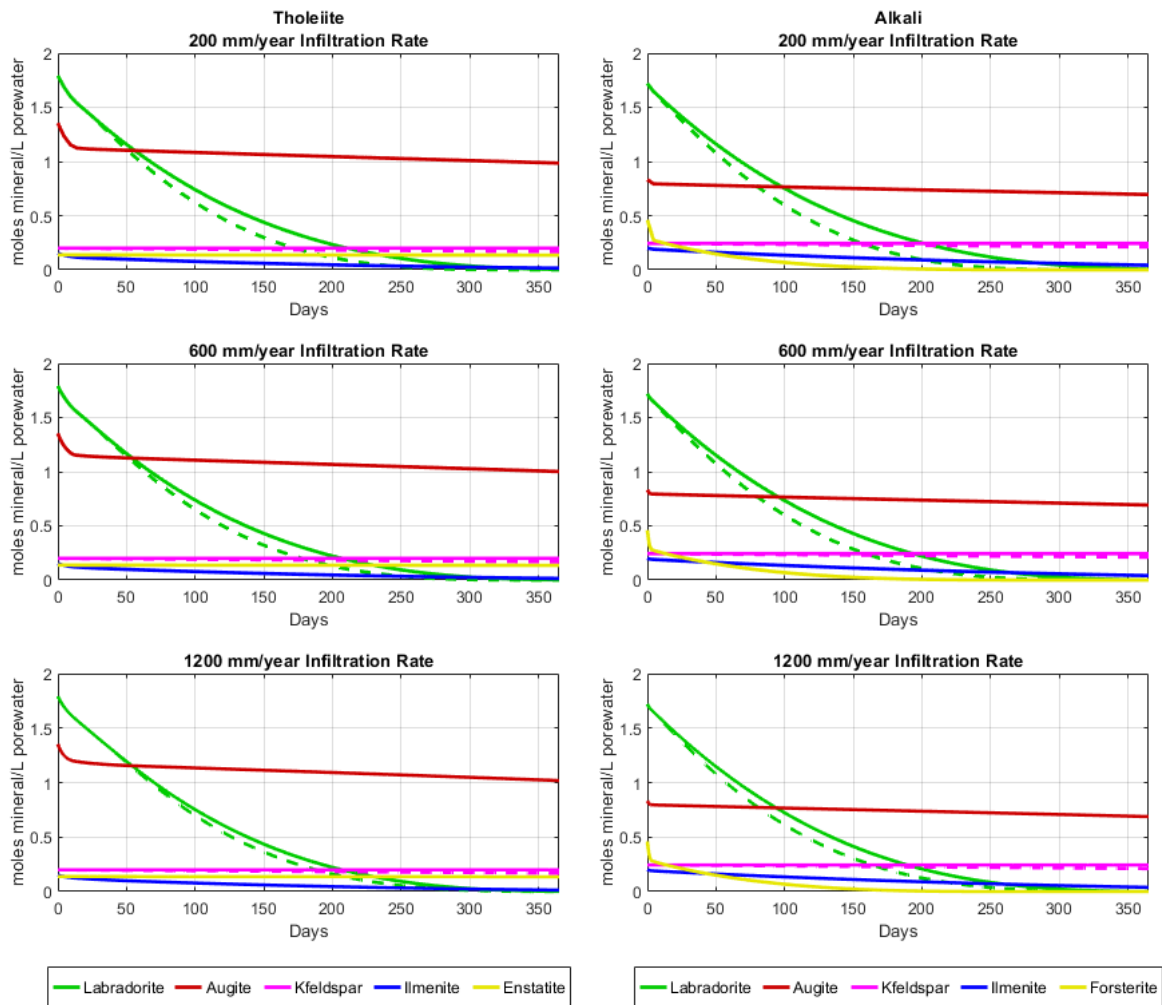
Figure S6. *Reactive transport model (RTM) sensitivity analyses of the affinity term during basalt weathering in agricultural soil.* Weathering depletion of initial basaltic mineral masses (expressed in moles of remaining basaltic mineral in contact with litres of soil pore-water) are shown for tholeiitic basalt (left hand panels) and alkaline basalt (right hand panels). Results are shown for three infiltrations rates of 200 mm yr^{-1}, 600 mm yr^{-1} and 1200 mm yr^{-1}. Results are plotted for a period of one year with (solid line) and without (dashed line) implementing the chemical affinity term to account for kinetic inhibition of dissolution. Only labradorite (green line) in these basalts exhibits noticeable effects. This is greatest during the first 100 days, especially under a low flow rate (200 mm yr^{-1} top panels) because there is little dilution of the weathered products, resulting in higher pore water concentrations exerting a stronger affinity effect. At the two higher flow rates, shorter residence times result in less solute accumulation within the soil profile and a weaker chemical affinity effect. Consequently, labradorite dissolves to completion after 365 days, and the results of the simulations that include and neglect affinity effects converge. Kfeldspar also exerts a minor affinity effect but is present in such low concentrations that its influence on the basalt-porewater system can be considered to be negligible. All simulations used the same single particle size (10 μm diameter) and were run at 25 °C.

20
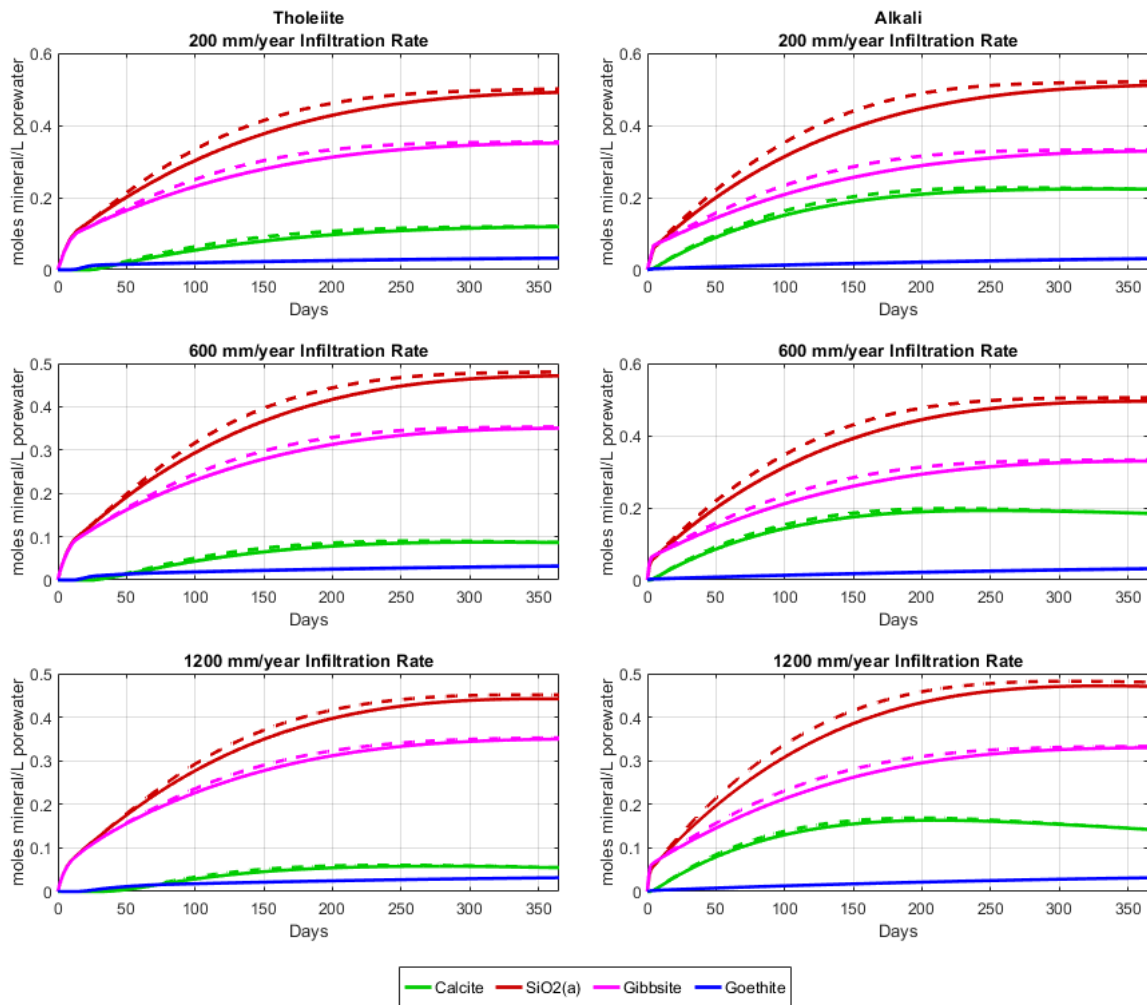
Figure S7. *Reactive Transport Model (RTM) simulated precipitation of secondary mineral phases during basalt weathering.* Simulated mass of the secondary mineral phases of calcite, amorphous silica (SiO$_2$(a)), gibbsite and geothite, precipitating during basalt weathering. Results are expressed in terms of moles of mineral precipitated per litre of soil pore waters, for the same set of RTM simulations as given in Fig. S6. Results are shown for with (solid line) and without (dashed line) including the chemical affinity term for dissolution inhibition of the primary minerals (see Methods Section 2.4). These results show that when affinity effects for primary minerals are neglected, that secondary mineral accumulation is more rapid. All simulations used the same single particle size (10 µm diameter) and were run at 25 °C.
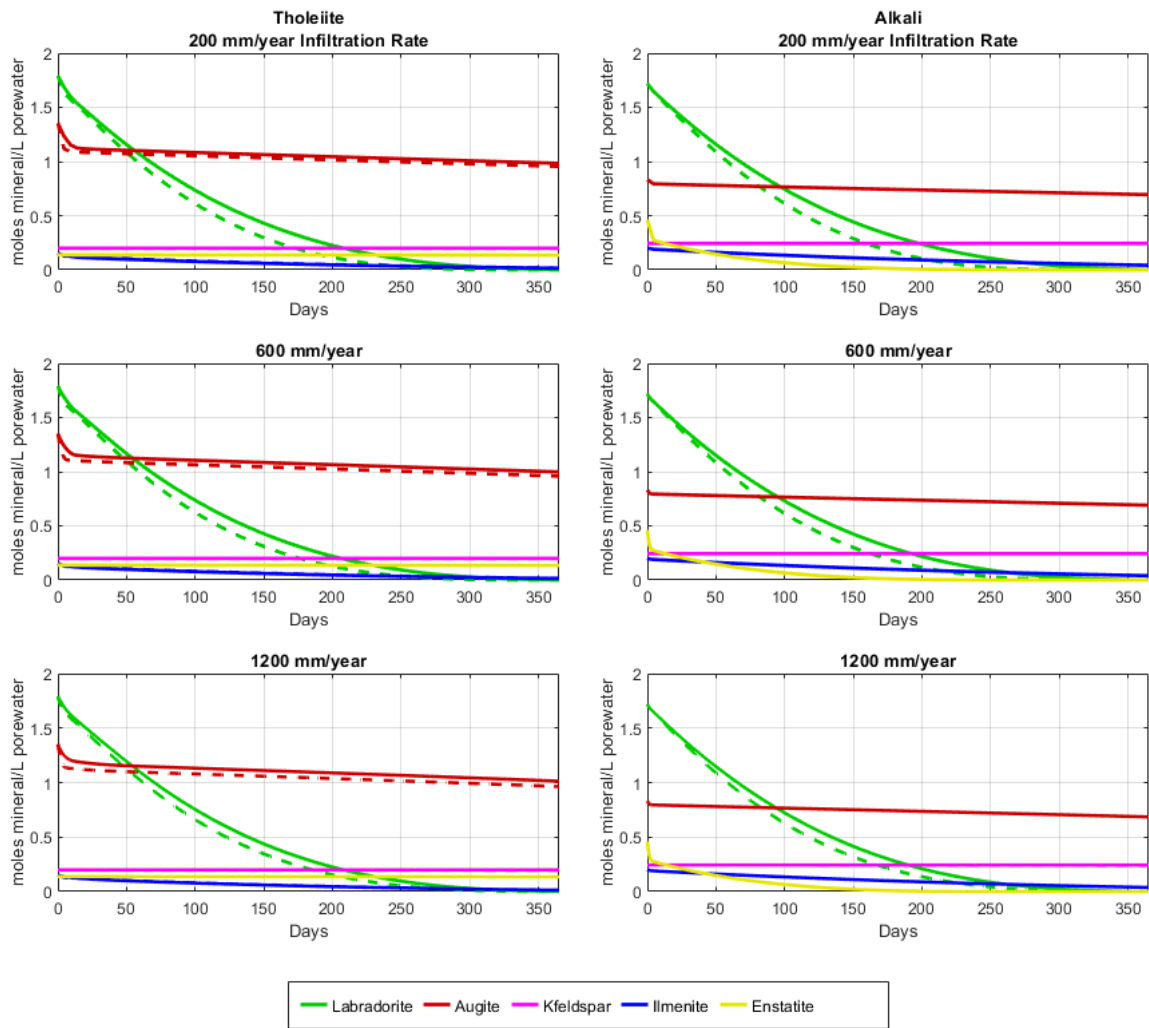
Figure S8. *Reactive transport model (RTM) sensitivity analyses to kaolinite formation during basalt weathering in agricultural soil.* Effect of clay (kaolinite) formation on weathering depletion of initial basaltic mineral masses (expressed in moles of remaining basaltic mineral in contact with litres of soil pore-water) are shown for tholeiitic basalt (left hand panels) and alkaline basalt (right hand panels). Results are shown for three infiltrations rates of 200 mm yr^{-1}, 600 mm yr^{-1} and 1200 mm yr^{-1}. Results are plotted for a period of one year with (dashed line) and without (solid line) kaolinite formation. Results indicate allowing kaolinite formation accelerates dissolution of labradorite (dashed vs solid green lines) and augite (dashed vs solid red lines) through suppression of Al ion activity in solution resulting in less kinetic inhibition of the dissolution reactions.
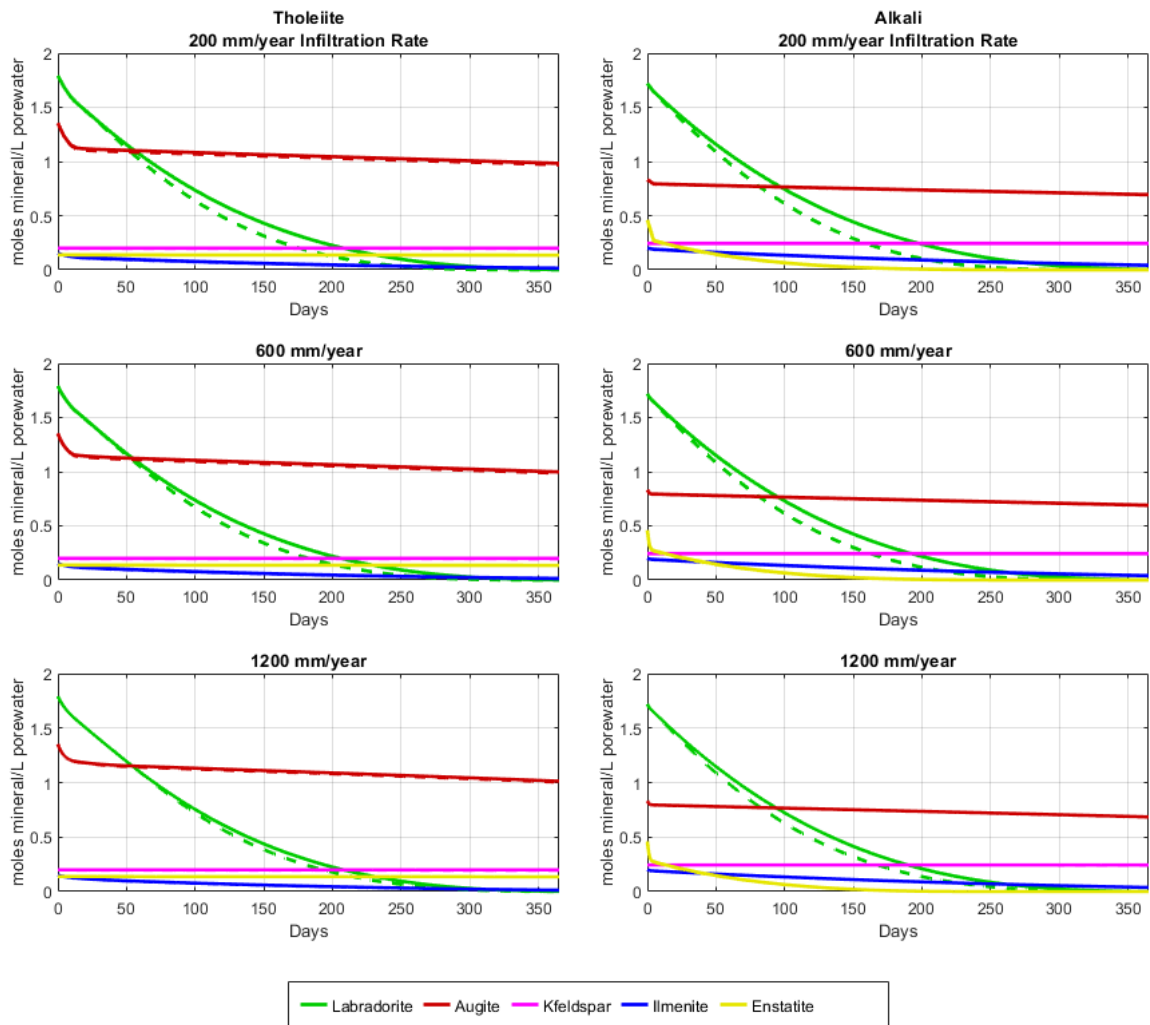
Figure S9. *Reactive transport model (RTM) sensitivity analyses to smectite (montmorillonite) formation during basalt weathering in agricultural soil.* Effect of smectite clay montmorillonite formation on weathering depletion of initial basaltic mineral masses (expressed in moles of remaining basaltic mineral in contact with litres of soil pore-water) are shown for tholeiitic basalt (left hand panels) and alkaline basalt (right hand panels). Results are shown for three infiltrations rates of 200 mm yr^{-1}, 600 mm yr^{-1} and 1200 mm yr^{-1}. Results are plotted for a period of one year with (dashed line) and without (solid line) montmorillonite formation. Results indicate allowing montmorillonite formation accelerates dissolution of labradorite (dashed vs solid green lines) and augite (dashed vs solid red lines) through suppression of Al ion activity in solution resulting in less kinetic inhibition of the dissolution reactions.
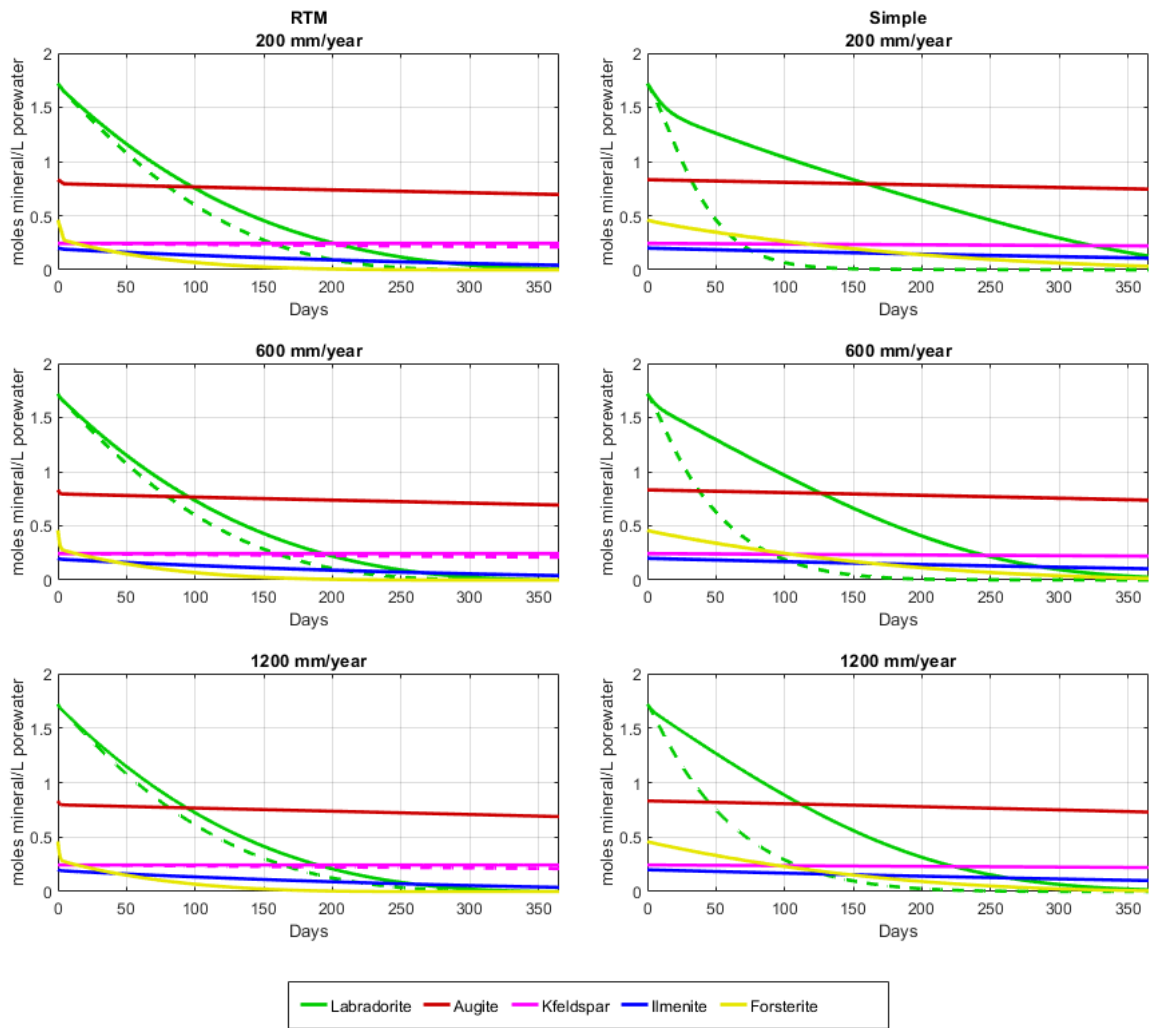
Figure S10. *Comparison of RTM and performance model results for rates of mineral weathering for alkali basalt.* Results for the reactive transport model (RTM) with the full rate equation and geochemical speciation including calculation of the effects of chemical affinity (left hand plots) and the calibrated performance ('simple') model that includes affinity effects with a simplified mass transfer inhibition term for weathering of individual minerals (right hand plots). The results show close correspondence between models across all three flow regimes. All simulations used the same single particle size (10 µm diameter) and were run at 25 °C.
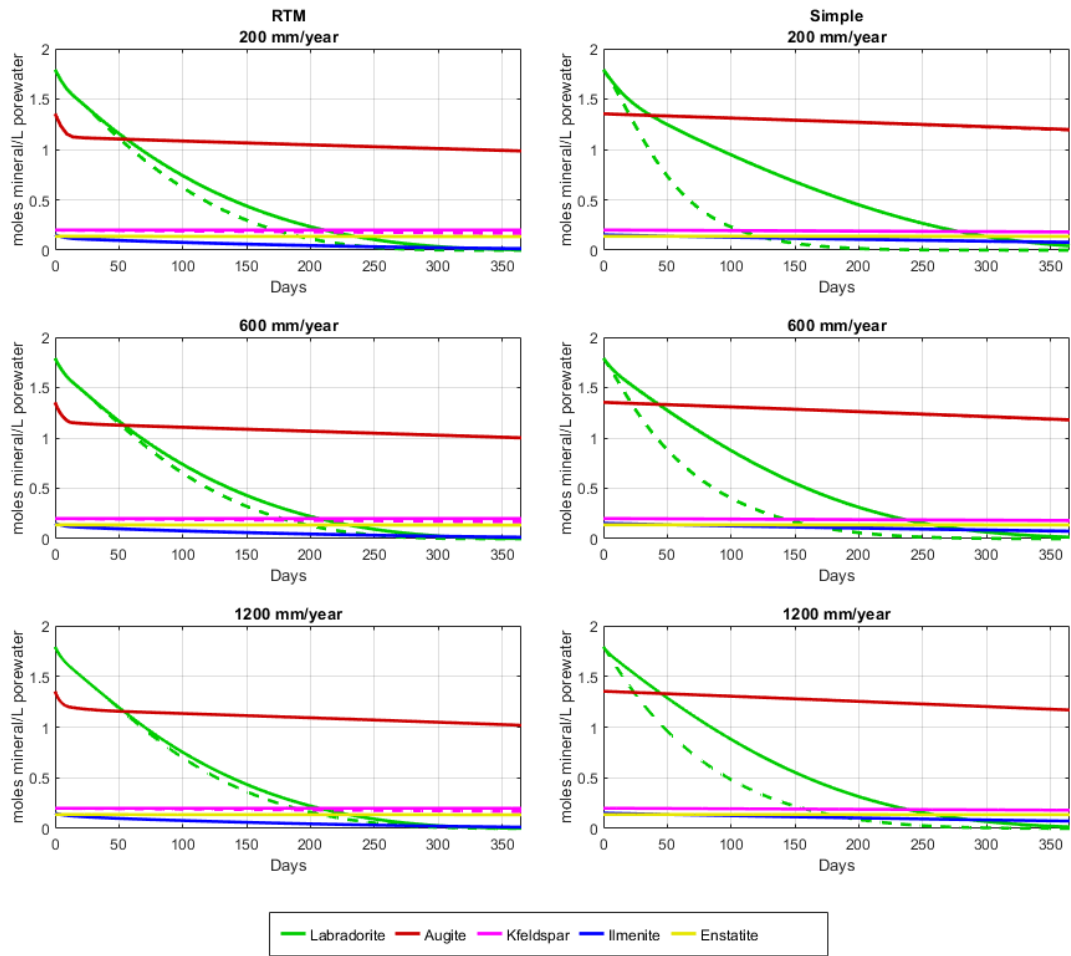
Figure S11. *Comparison of RTM and performance model results for rates of mineral weathering for tholetiic basalt.* Results for the reactive transport model (RTM) with the full rate equation and geochemical speciation including calculation of the effects of chemical affinity (left hand plots) and the calibrated performance model ('simple') that includes affinity effects with a simplified mass transfer inhibition term for weathering of individual minerals (right hand plots). The results show close correspondence between models across all three flow regimes. All simulations used the same single particle size (10 µm diameter) and were run at 25 °C.
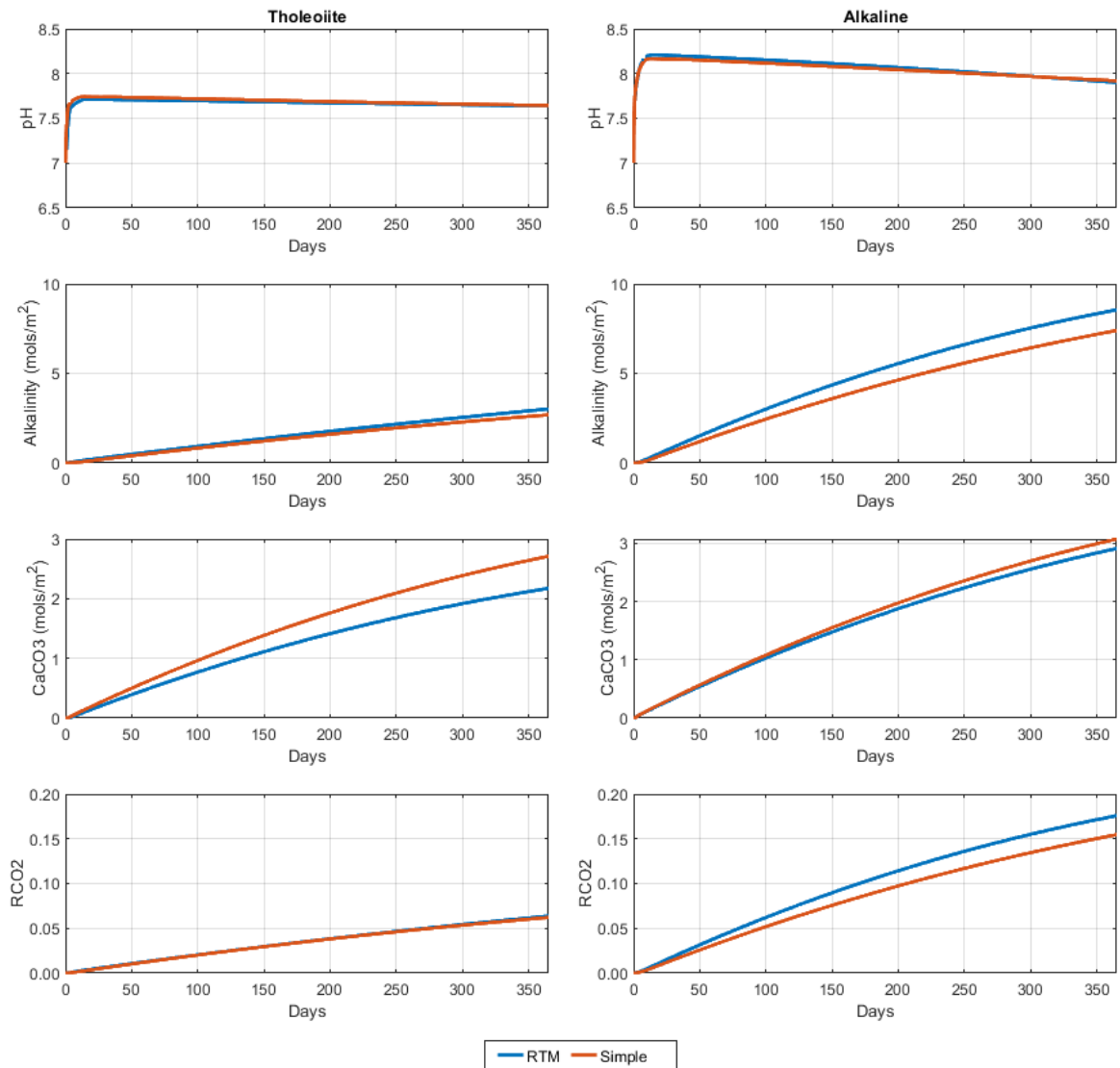
Figure S12 *Comparison of pH and carbon removal systems in the RTM and peformance model.*
Comparison shows the close similarities between the simulated changes in pH, alkalinity flux (Ca^{2+}+
Mg^{2+} + Na^+ + K^+), formation of pedogenic carbonate ($CaCO_3$) and efficiency of CO_2 removal (RCO_2) for
the reactive transport model ('RTM') and the performance model ('simple'). Left-hand plots for the
tholeiitic basalt, right-hand plots for the alkali basalt. All simulations used the same *p*80 particle size
(100 μm diameter) and were run at 20 °C; RTM simulations conducted without cation exchanges to
account for saturation following multi-year basalt applications.

26
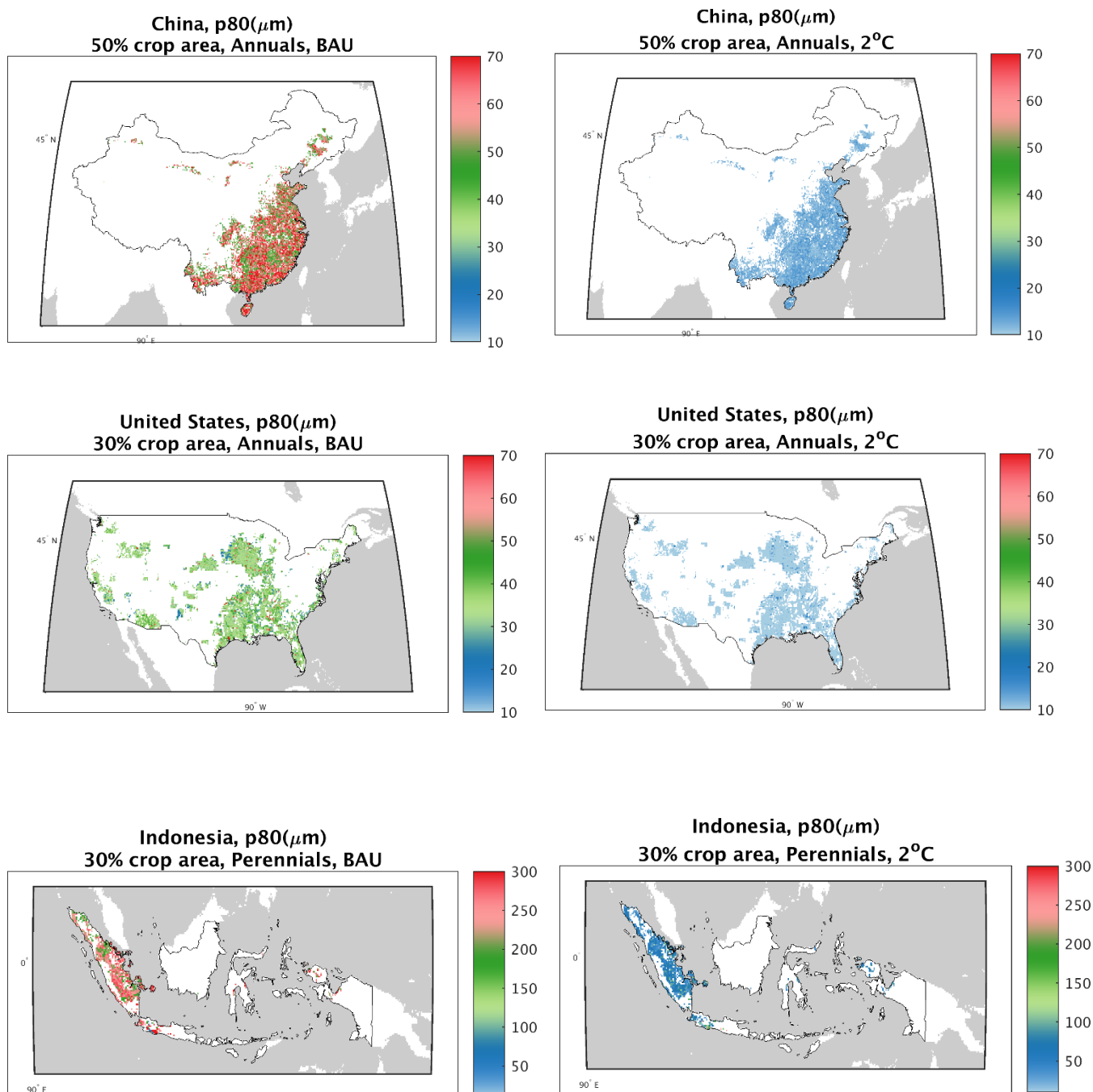
Figure S13. *Optimal particle size distributions for croplands.* Values of particle size are *p*80s; i.e., 80% of particles are less than or equal to this diameter (μm). Illustrative maps for the simulated particle size *p*80s for China (top maps), USA (middle maps) and Indonesia (lower maps). Left hand maps are for the business-as-usual energy policy (BAU) scenario simulations and right hand maps for the 2°C energy polciy scenario simulations. Under the 2°C scenario, low carbon energy production used for rock ginding allows a simulated reduction in *p*80s for the same cropland fractional area.
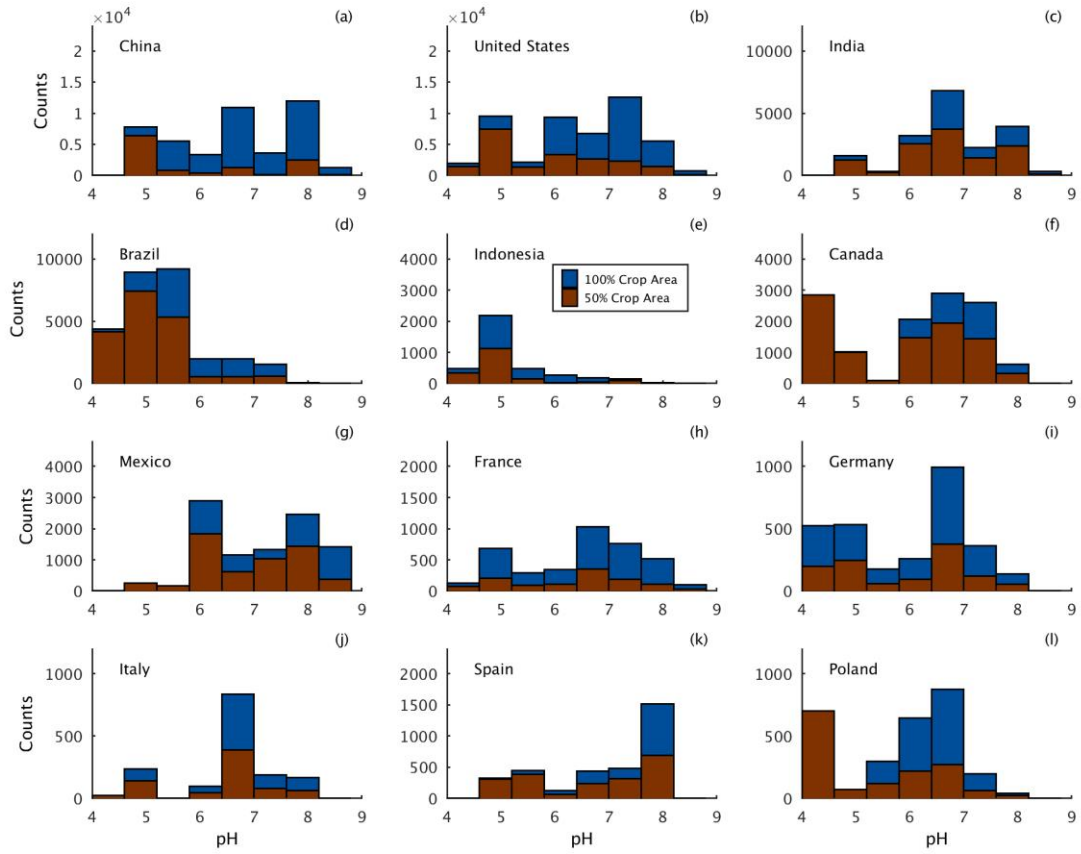
Figure S14. *Frequency histograms for national initial soil surface (0-30cm) pH.* Histograms show the distribution of initial top soil pH for 50% (red bars only), and 100 % of crop grid cells (red and blue bars). Datasets are shown for the 12 nations considered in our analysis, see Tabel S15 for sources of global soil pH database and cropland distributions.
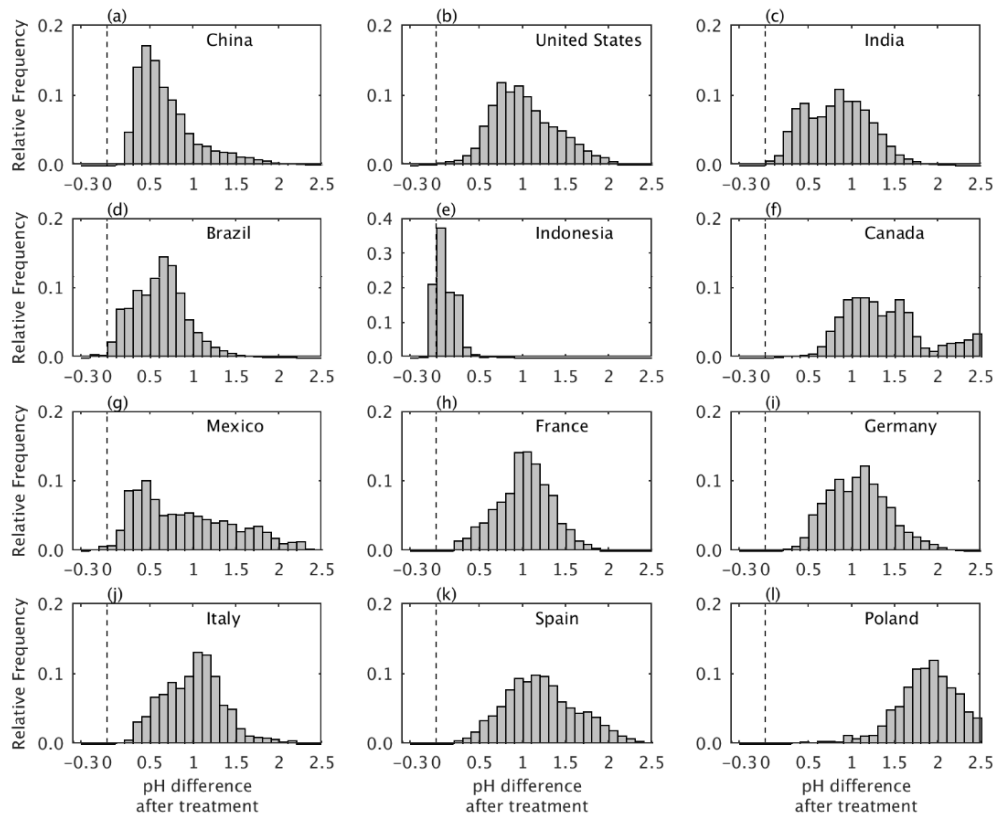
Figure S15. *Soil grid cell pH response to enhanced weathering with basalt rock dust.* Results are shown for the 12 nations considered in our analysis with 50% cropland deployment. Results are expressed as the simulated change in initial soil pH after 10 years of basalt application for the business-usual energy policy senario. Results for the 2°C energy policy scenario are very similar. The extent to which simulated pH increases promote or adversely affect crop production depends on the initial topsoil pH, crop functional traits, weathering rates, climate, flushing rates and fertiliser treatments.
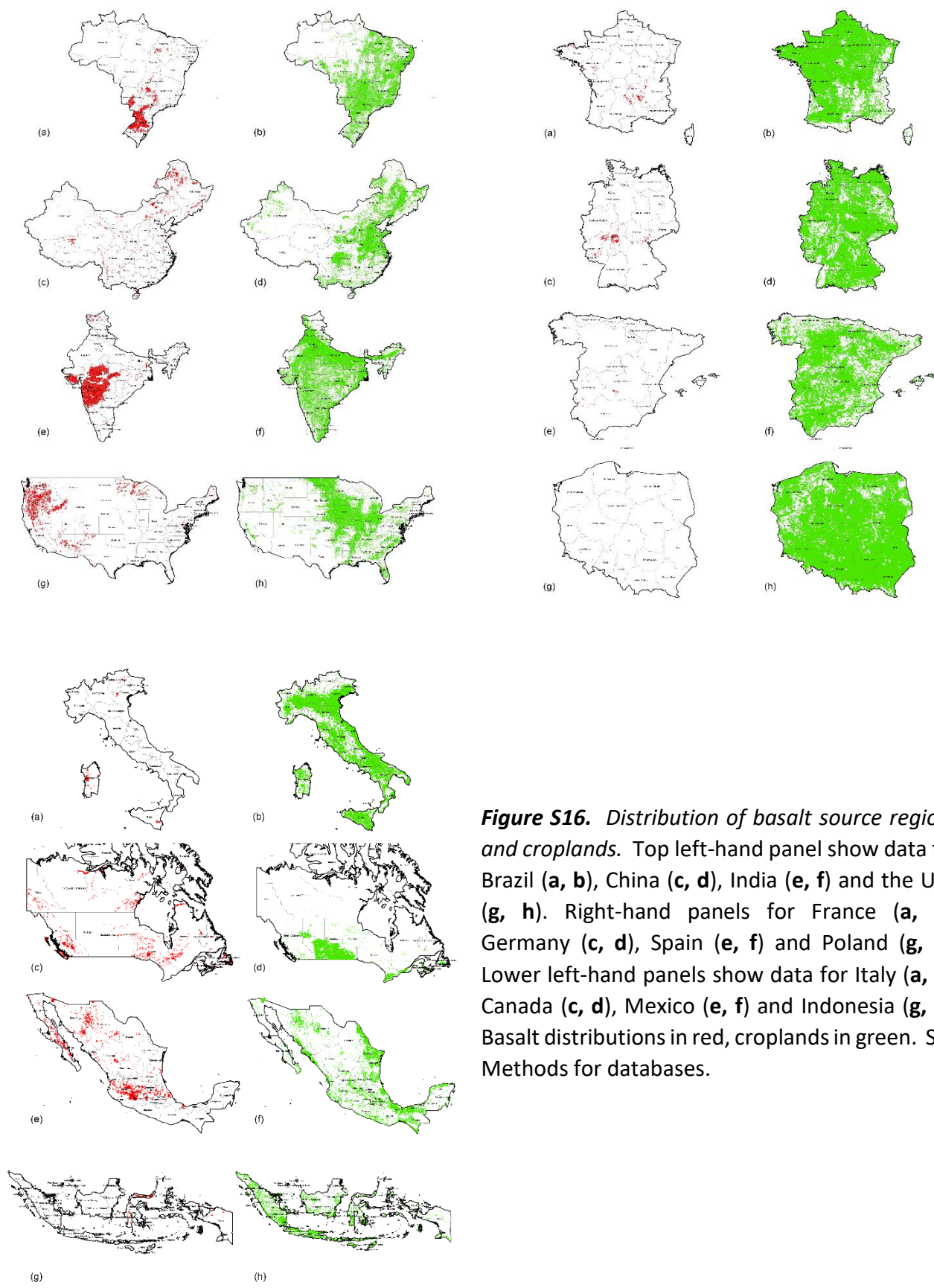
Figure S16. *Distribution of basalt source regions and croplands.* Top left-hand panel show data for Brazil (**a, b**), China (**c, d**), India (**e, f**) and the USA (**g, h**). Right-hand panels for France (**a, b**), Germany (**c, d**), Spain (**e, f**) and Poland (**g, h**). Lower left-hand panels show data for Italy (**a, b**), Canada (**c, d**), Mexico (**e, f**) and Indonesia (**g, h**). Basalt distributions in red, croplands in green. See Methods for databases.
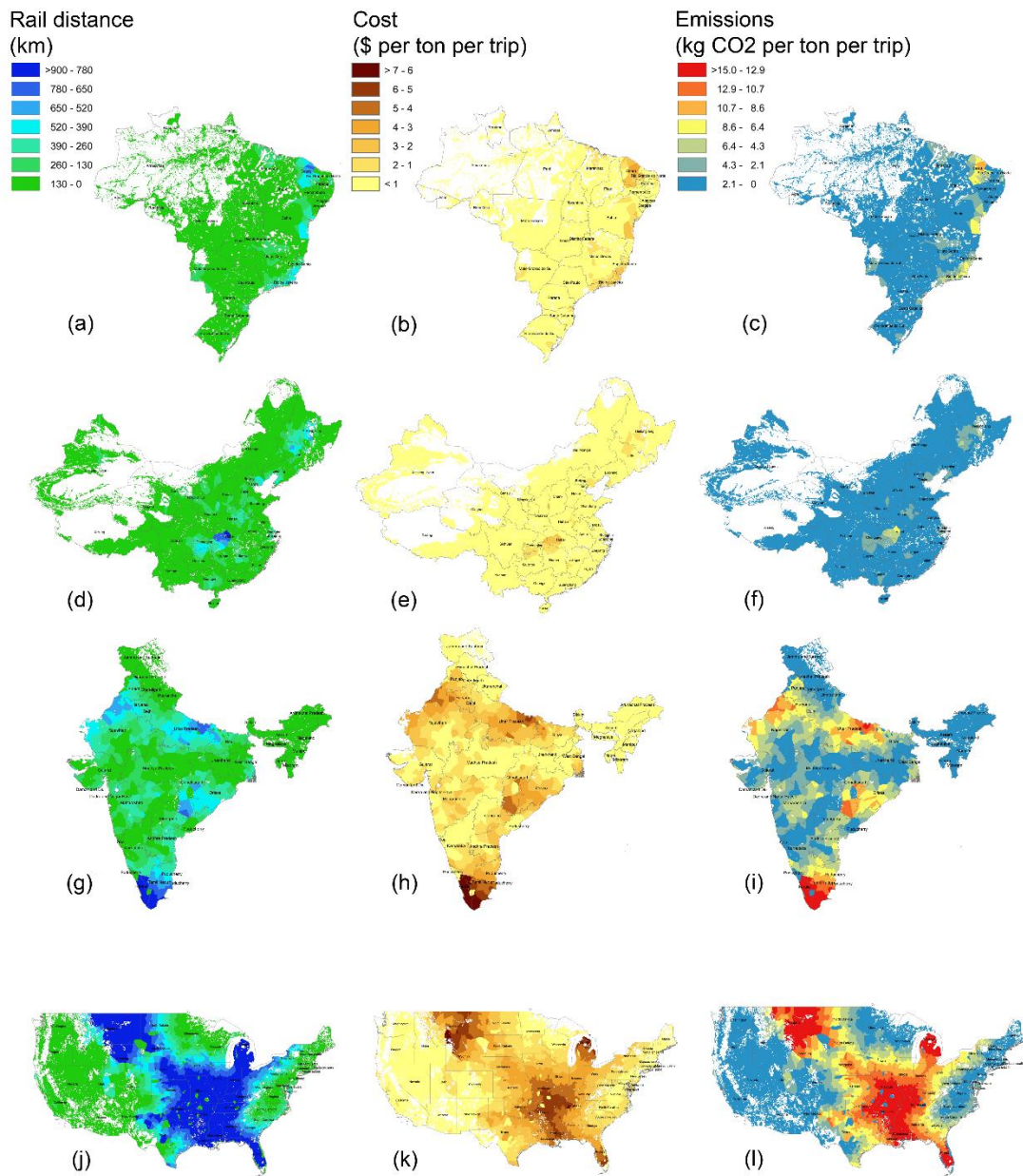
Figure S17. *Calculated basalt source-to-field rail distances, costs and CO₂ emissions, part 1.* Maps show data for Brazil (**a-c**), China (**d-f**), India (**g-i**) and the USA (**j-l**). Table S10 provides summary statistics for distances, costs and emissions of nations.
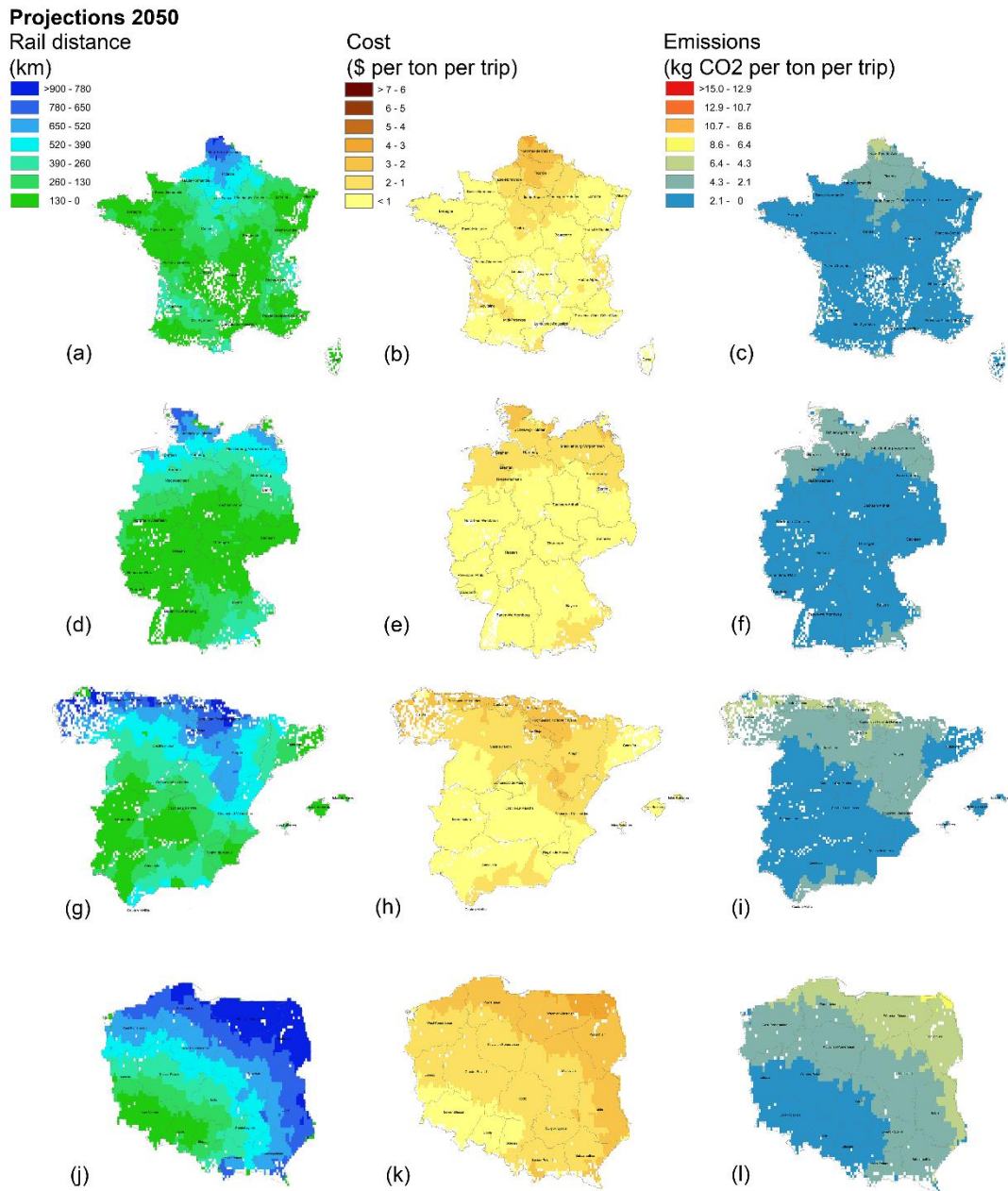
Figure S18. *Calculated basalt source-to-field rail distances, costs and CO₂ emissions, part 2.* Maps show data for France (**a-c**), Germany (**d-f**), Spain (**g-i**) and Poland (**j-l**). Table S10 provides summary statistics for distances, costs and emissions of nations.

Projections 2050

Rail distance (km)
- >900 - 780
- 780 - 650
- 650 - 520
- 520 - 390
- 390 - 260
- 260 - 130
- 130 - 0

Cost ($ per ton per trip)
- > 7 - 6
- 6 - 5
- 5 - 4
- 4 - 3
- 3 - 2
- 2 - 1
- < 1

Emissions (kg CO2 per ton per trip)
- >15.0 - 12.9
- 12.9 - 10.7
- 10.7 - 8.6
- 8.6 - 6.4
- 6.4 - 4.3
- 4.3 - 2.1
- 2.1 - 0

(a)   (b)   (c)

(d)   (e)   (f)

(g)   (h)   (i)

(j)   (k)   (l)
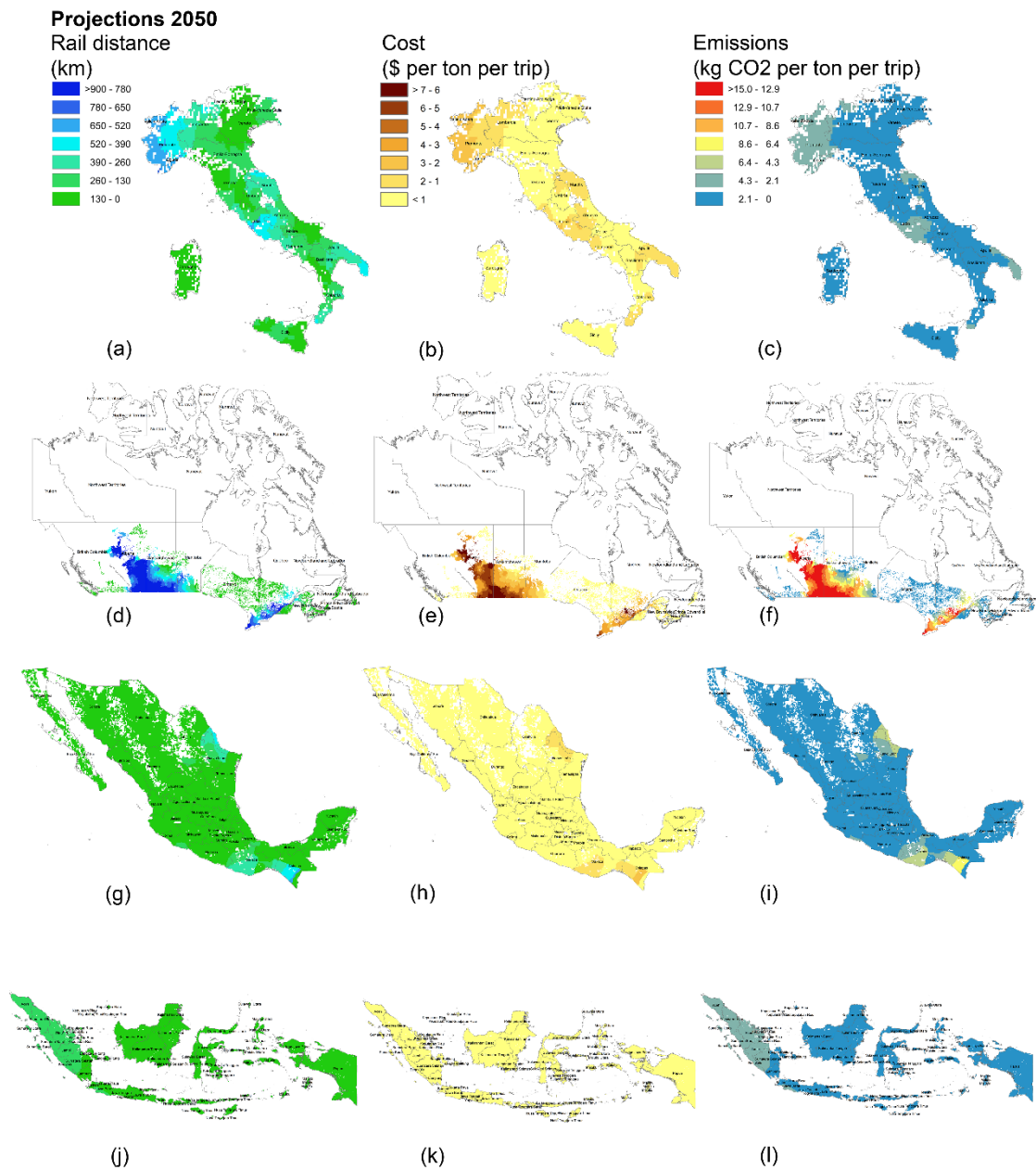
Figure S19. *Calculated basalt source-to-field rail distances, costs and CO$_2$ emissions, part 3.* Maps show data for Italy (**a-c**), Canada (**d-f**), Mexico (**g-i**) and Indonesia (**j-l**). Table S10 provides summary statistics for distances, costs and emissions of nations.

Projections scenario 1 for 2050

Roads distance
(km)

- >900 - 780
- 780 - 650
- 650 - 520
- 520 - 390
- 390 - 260
- 260 - 130
- 130 - 0

Cost
($ per ton per trip)

- > 7 - 6
- 6 - 5
- 5 - 4
- 4 - 3
- 3 - 2
- 2 - 1
- < 1

Emissions
(kg CO2 per ton per trip)

- >15.0 - 12.9
- 12.9 - 10.7
- 10.7 - 8.6
- 8.6 - 6.4
- 6.4 - 4.3
- 4.3 - 2.1
- 2.1 - 0

(a)

(b)

(c)

(d)

(e)

(f)

(g)

(h)

(i)

(j)

(k)

(l)
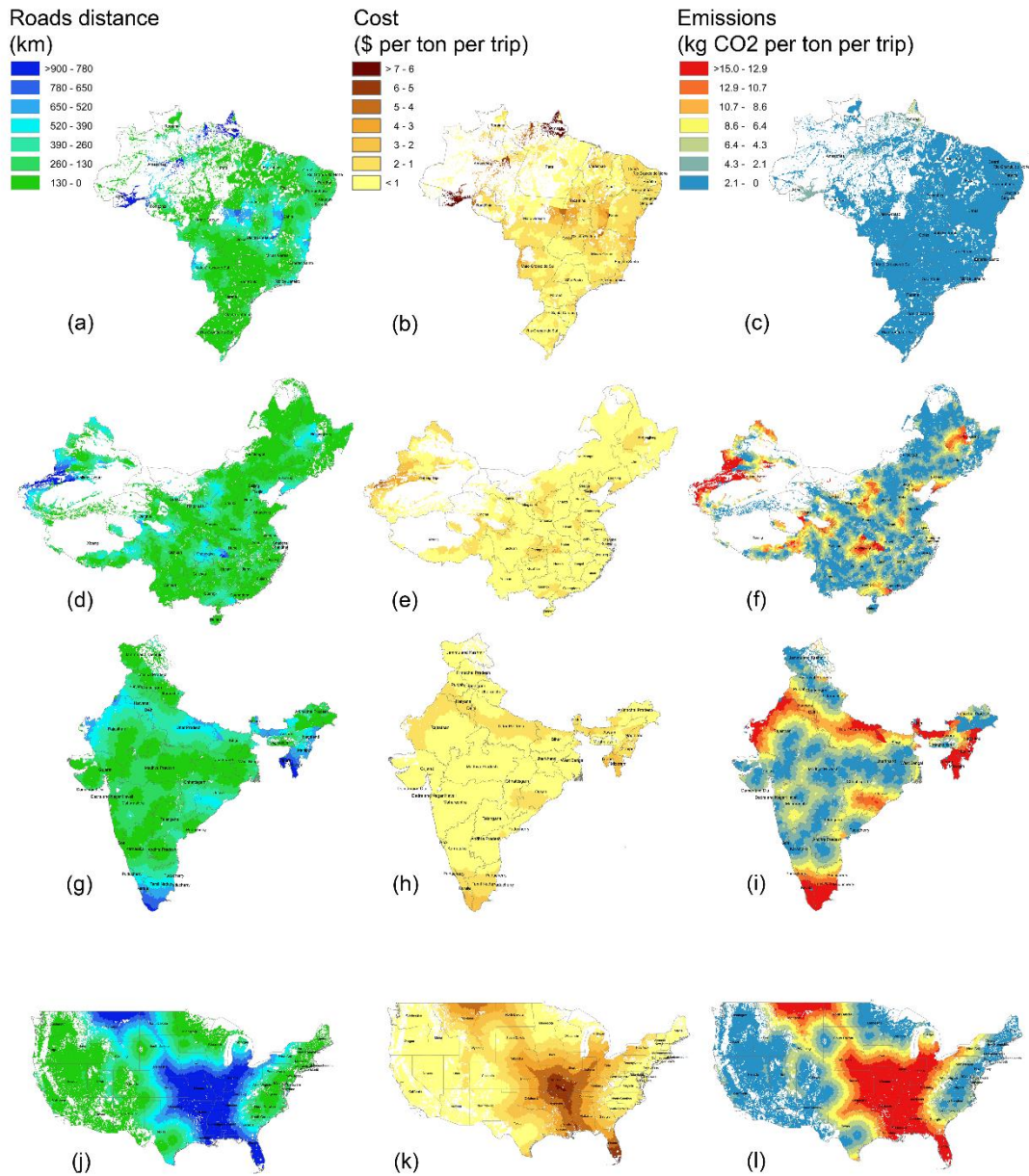
Figure S20. *Calculated basalt source-to-field road distances, costs and CO₂ emissions for the business-as-usual scenario, part 1.* Maps show data for Brazil (**a-c**), China (**d-f**), India (**g-i)** and the USA (**j-l**). Table S11 provides summary statistics for distances, costs and emissions of nations.
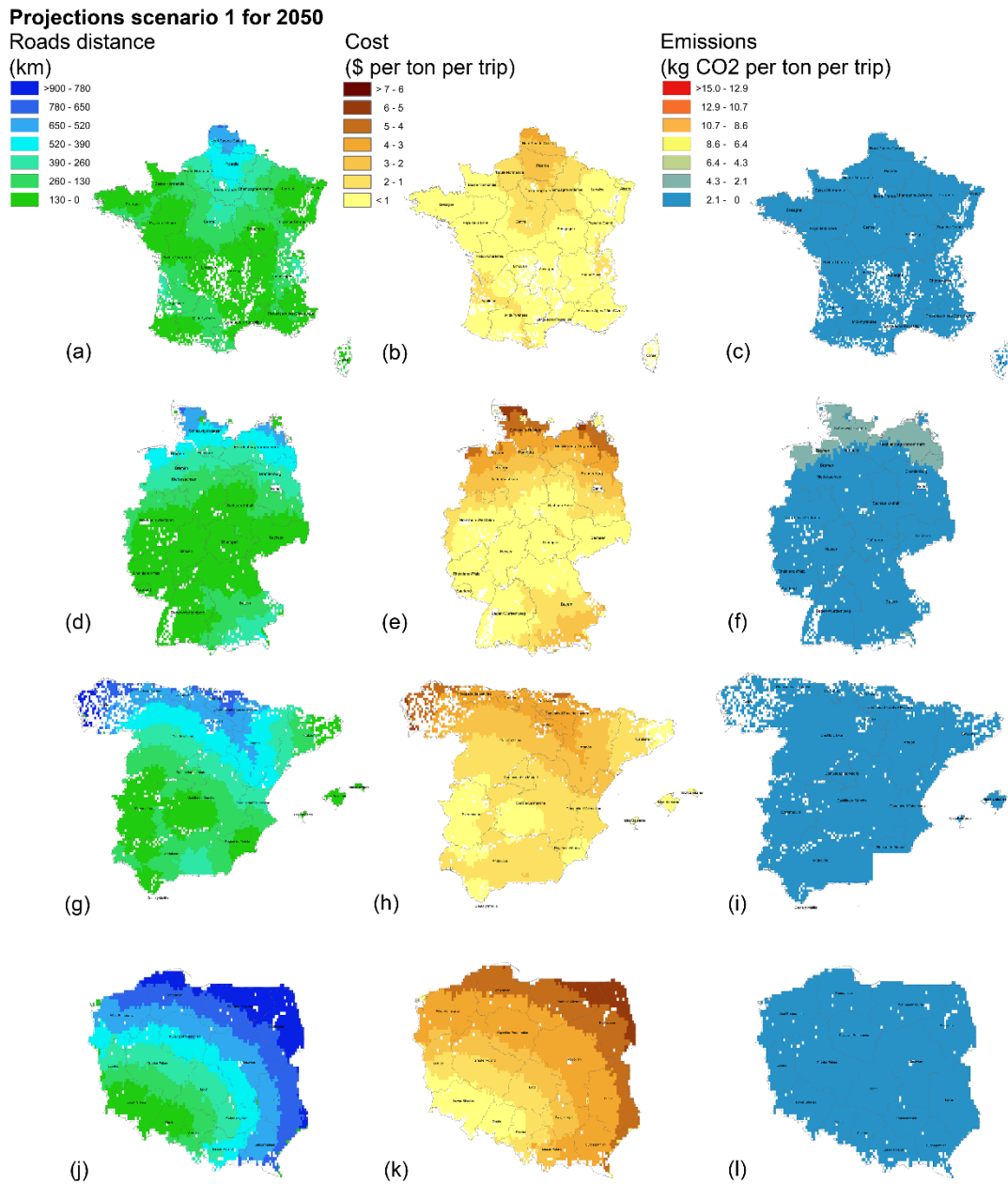
Figure S21. *Calculated basalt source-to-field road distances, costs and CO₂ emissions for the business-as-usual scenario, part 2.* Maps show data for France (**a-c**), Germany (**d-f**), Spain (**g-i**) and Poland (**j-l**). Table S11 provides summary statistics for distances, costs and emissions of nations.

Projections scenario 1 for 2050

Roads distance (km)
- >900 - 780
- 780 - 650
- 650 - 520
- 520 - 390
- 390 - 260
- 260 - 130
- 130 - 0

Cost ($ per ton per trip)
- > 7 - 6
- 6 - 5
- 5 - 4
- 4 - 3
- 3 - 2
- 2 - 1
- < 1

Emissions (kg CO2 per ton per trip)
- >15.0 - 12.9
- 12.9 - 10.7
- 10.7 - 8.6
- 8.6 - 6.4
- 6.4 - 4.3
- 4.3 - 2.1
- 2.1 - 0

(a)   (b)   (c)

(d)   (e)   (f)

(g)   (h)   (i)

(j)   (k)   (l)
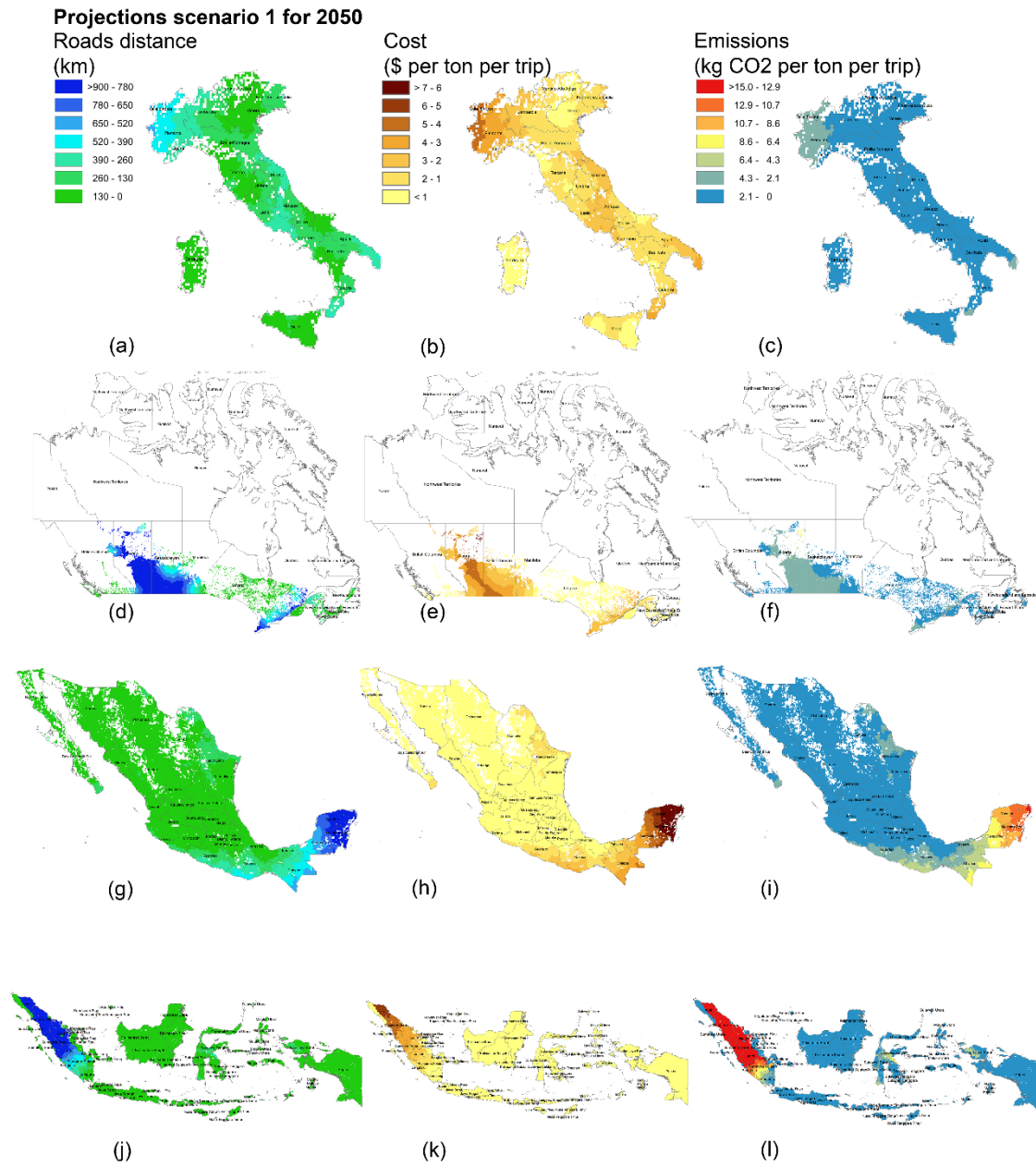
Figure S22. *Calculated basalt source-to-field road distances, costs and CO$_2$ emissions for the business-as-usual scenario, part 3.* Maps show data for Italy (**a-c**), Canada (**d-f**), Mexico (**g-i**) and Indonesia (**j-l**). Table S11 provides summary statistics for distances, costs and emissions of nations.

Projections scenario 2 for 2050

Roads distance (km)
- >900 - 780
- 780 - 650
- 650 - 520
- 520 - 390
- 390 - 260
- 260 - 130
- 130 - 0

Cost ($ per ton per trip)
- > 7 - 6
- 6 - 5
- 5 - 4
- 4 - 3
- 3 - 2
- 2 - 1
- < 1

Emissions (kg CO2 per ton per trip)
- >15.0 - 12.9
- 12.9 - 10.7
- 10.7 - 8.6
- 8.6 - 6.4
- 6.4 - 4.3
- 4.3 - 2.1
- 2.1 - 0
- 0 - -2.1
- -2.1 - -4.3

(a) (b) (c)

(d) (e) (f)

(g) (h) (i)

(j) (k) (l)
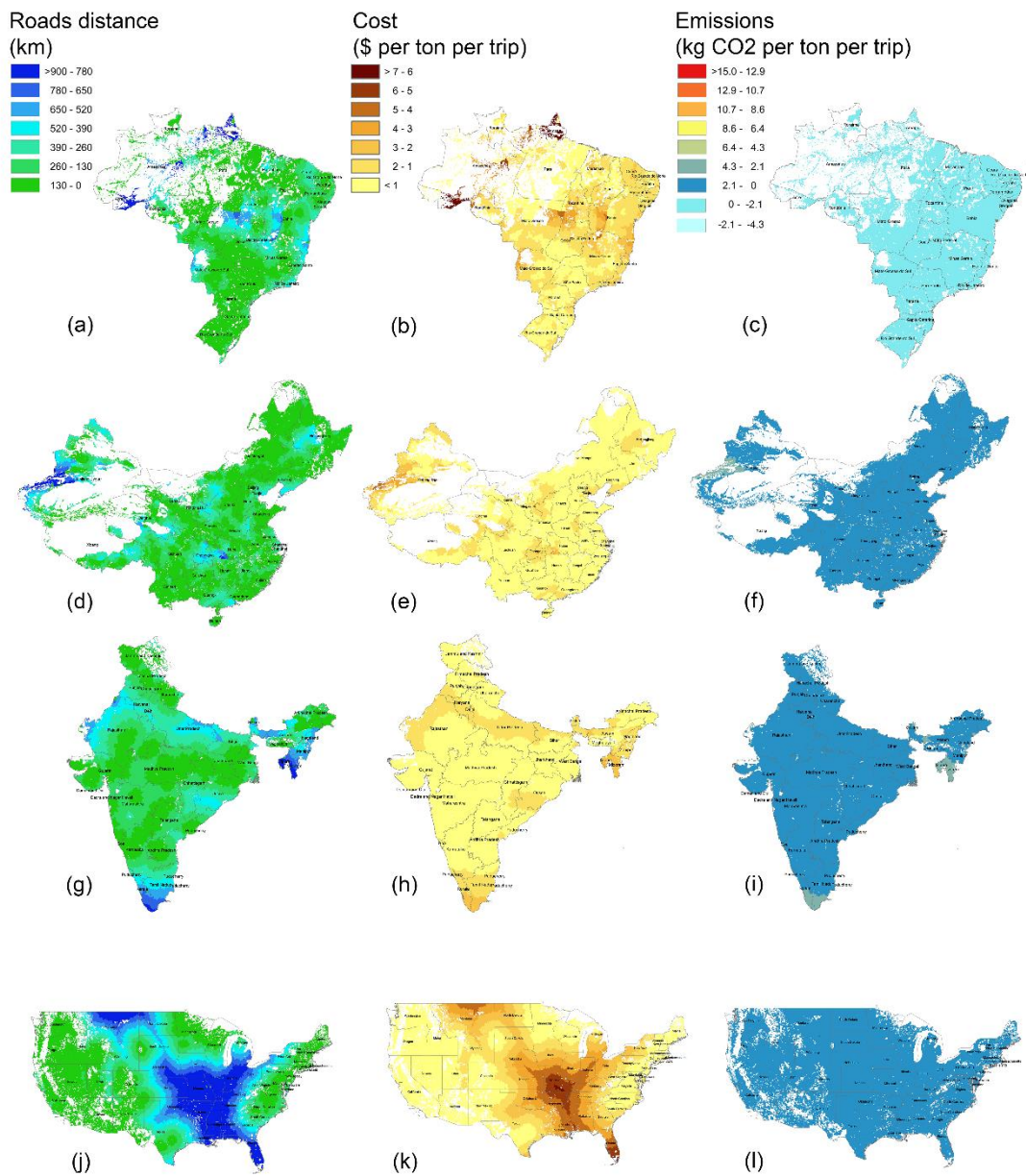
Figure S23. *Calculated basalt source-to-field road distances, costs and CO$_2$ emissions for the 2°C scenario, part 1.* Maps show data for Brazil (**a-c**), China (**d-f**), India (**g-i**) and the USA (**j-l**). Table S12 provides summary statistics for distances, costs and emissions of nations.

Projections scenario 2 for 2050

Roads distance (km)
- >900 - 780
- 780 - 650
- 650 - 520
- 520 - 390
- 390 - 260
- 260 - 130
- 130 - 0

Cost ($ per ton per trip)
- > 7 - 6
- 6 - 5
- 5 - 4
- 4 - 3
- 3 - 2
- 2 - 1
- < 1

Emissions (kg CO_2 per ton per trip)
- >15.0 - 12.9
- 12.9 - 10.7
- 10.7 - 8.6
- 8.6 - 6.4
- 6.4 - 4.3
- 4.3 - 2.1
- 2.1 - 0
- 0 - -2.1
- -2.1 - -4.3

(a) (b) (c) (d) (e) (f) (g) (h) (i) (j) (k) (l)
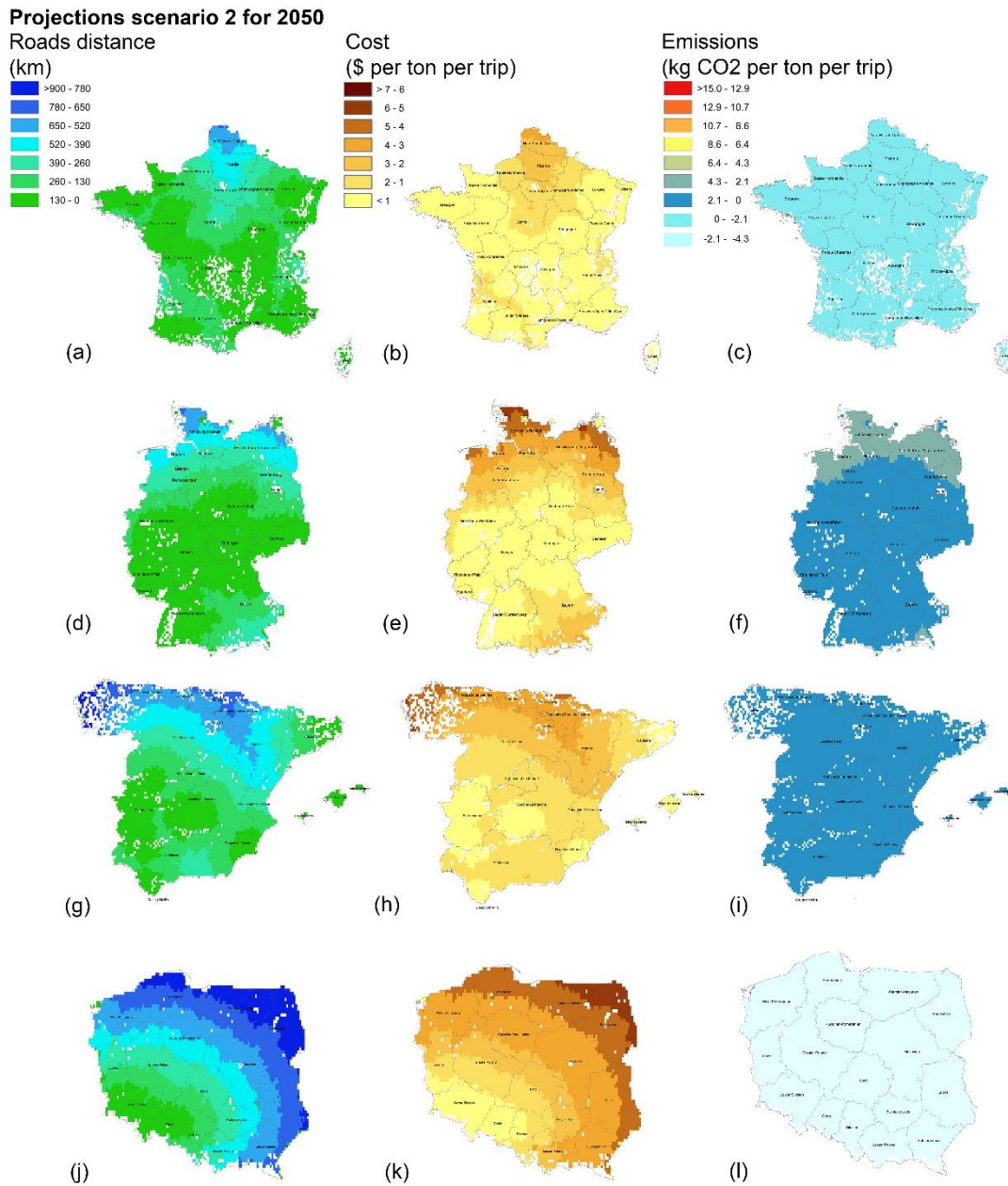
Figure S24. *Calculated basalt source-to-field road distances, costs and CO_2 emissions for 2°C scenario, part 2.* Maps show data for France (**a-c**), Germany (**d-f**), Spain (**g-i**) and Poland (**j-l**). Table S12 provides summary statistics for distances, costs and emissions of nations.

Projections scenario 2 for 2050

Roads distance (km)
- >900 - 780
- 780 - 650
- 650 - 520
- 520 - 390
- 390 - 260
- 260 - 130
- 130 - 0

Cost ($ per ton per trip)
- > 7 - 6
- 6 - 5
- 5 - 4
- 4 - 3
- 3 - 2
- 2 - 1
- < 1

Emissions (kg CO2 per ton per trip)
- >15.0 - 12.9
- 12.9 - 10.7
- 10.7 - 8.6
- 8.6 - 6.4
- 6.4 - 4.3
- 4.3 - 2.1
- 2.1 - 0
- 0 - -2.1
- -2.1 - -4.3

(a) (b) (c)
(d) (e) (f)
(g) (h) (i)
(j) (k) (l)
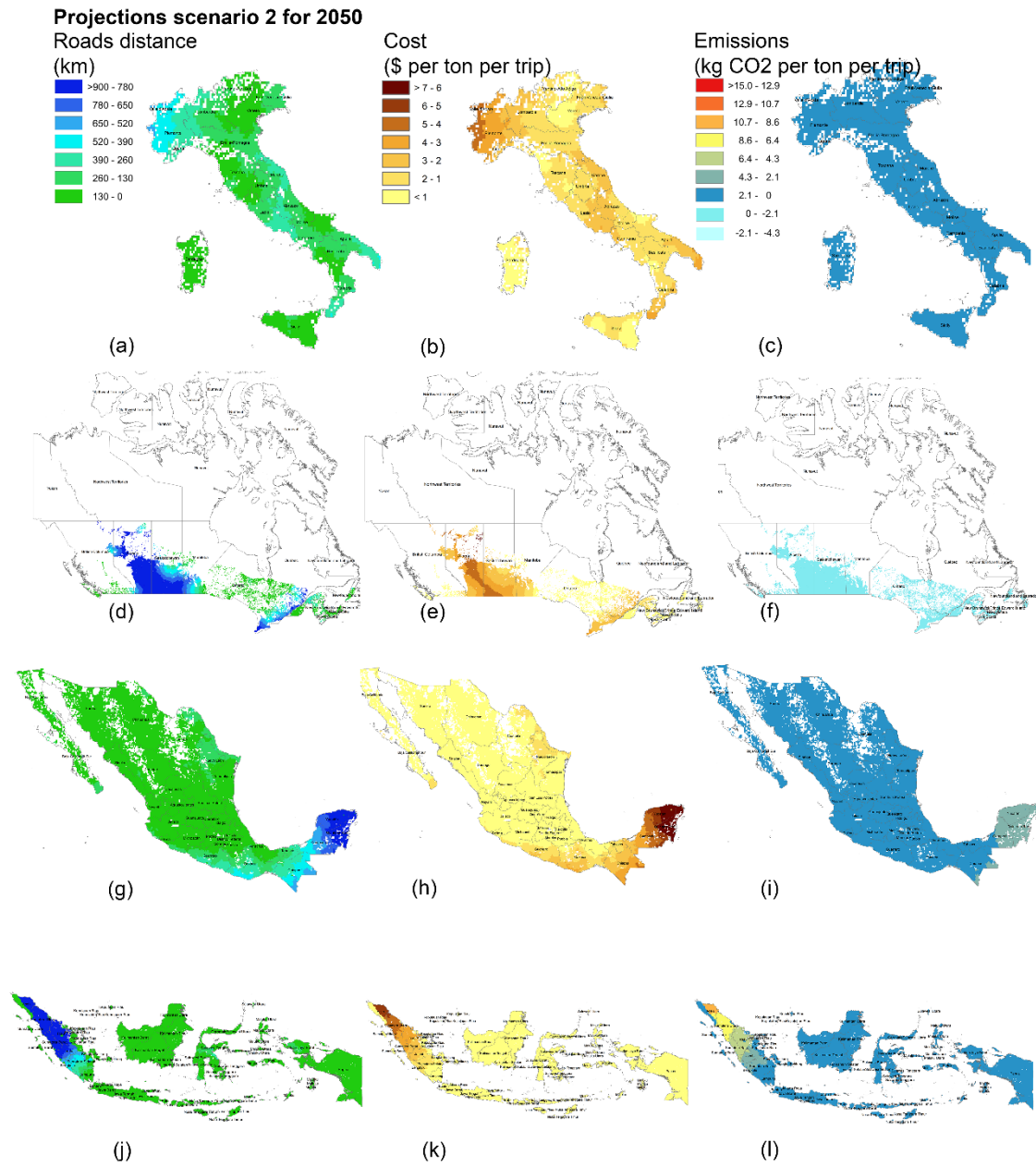
Figure S25. *Calculated basalt source-to-field road distances, costs and CO$_2$ emissions for the 2°C scenario, part 3.* Maps show data for Italy (**a-c**), Canada (**d-f**), Mexico (**g-i**) and Indonesia (**j-l**). Table S12 provides summary statistics for distances, costs and emissions of nations.

Table S1. *Mineral weight fractions of the basalt formulations.* Relatively unreactive mineral components, e.g., quartz, are not included[8,52].

Basalt formulation	Mineral	Weight-fractions
Normal Alkali-Basalt	Labradorite	0.43
(faster weathering)	Augite	0.21
	Forsterite	0.12
	Kfeldspar	0.06
	Fayalite	0.05
	Ilmenite	0.05
	Total	0.91
Normal Tholeiitic basalt	Augite	0.34
(slower weathering)	Enstatite	0.03
	Kfeldspar	0.05
	Labradorite	0.45
	Ilmenite	0.04
	Total	0.91

Table S2. *Mineral chemical characteristics.*

Basalt Formulation	Mineral	Chemical Formula	Molecular Mass (g/mol)
Normal-Alkali-Basalt	Labradorite	$Ca_{0.6}Na_{0.4}Al_{1.6}Si_{2.4}O_8$	271.937
(faster-weathering)	Augite	$Ca_{0.9}Mg_{0.9}Na_{0.1}Al_{0.4}Fe_{0.2}Si_{1.9}O_6$	236.371
	Forsterite	Mg^2SiO_4	140.708
	Kfeldspar	$KAlSi3O8$	278.35
	Fayalite	$Fe2SiO4$	203.777
	Ilmenite	$FeTiO3$	151.73
Normal-Tholeiite	Augite	$Ca_{0.9}Mg_{0.9}Na_{0.1}Al_{0.4}Fe_{0.2}Si_{1.9}O_6$	236.371
(slower-weathering)	Enstatite	$MgSiO3$	100.4
	Kfeldspar	$KAlSi3O8$	278.35
	Labradorite	$Ca_{0.6}Na_{0.4}Al_{1.6}Si_{2.4}O_8$	271.937
	Ilmenite	$FeTiO3$	151.73

Table S3. *Kinetic parameters of basaltic minerals.* logK is the log of the effective rate constant (mol $m^{-2}\,s^{-1}$), E_{app} is the apparent activation energy (kJ mol^{-1}), *n* is the reaction order of the weathering agents H^+, H_2O or OH^-, corresponding to acid, neutral and base kinetic parameters[8,52].

Basalt Formulation	Mineral	Acid kinetic parameters			Neutral kinetic parameters		Base kinetic parameters		
		logK	E_{app}	*n*	logK	E_{app}	logK	E_{app}	*n*
Normal-Alkali-Basalt (faster weathering)	Labradorite	-7.87	42.1	0.63	-10.91	45.2	-15.57	71	-0.57
	Augite	-6.82	78	0.7	-11.97	78		-	-
	Forsterite	-6.85	67.2	0.47	-10.64	79	-		
	Kfeldspar	10.06	51.7	0.5	-12.41	38	-21.2	94.1	-0.82
	Fayalite	-	-	-	-	-	-	-	-
	Ilmenite	-8.35	37.9	0.42	-11.16	37.9			
Normal-Tholeiite (slower weathering)	Augite	-6.82	78	0.7	-11.97	78	-	-	-
	Enstatite	-9.02	80	0.6	-12.72	80	-	-	-
	Kfeldspar	10.06	51.7	0.5	-12.41	38	-21.2	94.1	-0.82
	Labradorite	-7.87	42.1	0.63	-10.91	45.2	-15.57	71	-0.57
	Ilmenite	-8.35	37.9	0.42	-11.16	37.9	-	-	-

Table S4. *Characteristics of agricultural soil solution used for initializing PhreeqC simulations.* Cation and anion values from a compilation of acid surface soil solutions[53], and the cation exchange capacity determined from a compilation of agricultural soils for Europe[54,55], USA[56] and China[57,58].

Pore water pH	4.8
Mean cation exchange capacity (cmol$_c$/kg)	16.2
Mean ion conc.	
Ca^{2+} (μM	590
Mg^{2+} (μM)	420
K$^+$ (μM)	230
Na$^+$ (μM)	660
NH$_4^+$ (μM)	870
Al^{3+} (μM)	56
NO$_3$ (μM)	1100
SO$_4$ (μM)	310
Cl (μM)	1600
PO$_4$ (μM)	8.8
Si (μM)	580

Table S5. *Function parameters for NPP enhanced weathering by annual and perennial crops*

Parameter	Annual	Perennial
a	0.140386	0.065906
x_{norm}	3	18
b	3.54559	1.48934

Table S6. *Projected national emissions of CO_2 by different energy sources for 2050 (thousands of tonnes C yr^{-1}) for the business-as-usual scenario. Results from simulations in Ref[33].*

Source	China	India	USA	Brazil	Indonesia	Canada	Mexico	France	Italy	Germany	Spain	Poland
1 Power & transport	2458882	1002226	799232	25678	94193	20157	60927	1657	16698	38162	4598	1017
2 O. energy own use & tra	147552	79871	25185	8164	5942	9871	10952	3352	5352	10703	3236	1413
3 Hydrogen production	0	0	0	0	0	0	0	0	0	0	0	0
4 Iron & steel	226819	32709	9465	8773	988	2523	4029	2754	1009	2451	799	749
5 Non-ferrous metals	13917	6071	5051	12320	263	246	17	207	128	35	204	267
6 Chemicals	956	6559	36659	7688	738	3571	2978	2299	408	0	805	2695
7 Non-metallics nes	458685	16577	33972	3845	2891	120	14930	2537	2687	9119	4364	1733
8 Ore-extra.(non-energy)	40	484	0	3639	1184	8013	703	182	87	256	117	37
9 Food, drink & tob.	1248	449	19798	6553	582	0	336	1230	269	22	333	383
10 Tex., cloth. & footw.	1338	1363	2579	558	698	0	0	26	217	241	106	28
11 Paper & pulp	15	1233	6202	4239	1440	579	627	463	517	1.8	251	91
12 Engineering etc	268	676	5123	0	104	0	97	1547	2413	4103	1332	643
13 Other industry	1617	412794	732	4434	45426	12113	2976	370	239	1647	1637	203
14 Construction	1555	0	80	0	245	338	7	575	24	1724	169	71
15 Rail transport	771	3196	122	746	0	3040	273	51	40	109	32	24
16 Road transport	96798	333024	119150	111516	75796	19010	49010	6266	15583	17952	14059	10364
17 Air transport	8720	15177	65697	7314	4163	7477	4064	1638	736	666	1349	60
18 Other transp. serv.	1671	260	2343	2059	231	2326	0.064	949	1485	955	718	557
19 Households	7917	11014	82175	3633	4603	8893	388	2605	1883	9901	701	4192
20 Agriculture, forestry	3900	71980	511	9614	2033	679	915	2304	1654	1226	2665	1365
21 Fishing	0	0	0	0	0	0	0	213	164	0	0	1.9
22 Other final use	19250	19589	48972	1045	1094	17541	263	4235	3969	6852	839	1318
23 Non-energy use	0	0	0	0	0	0	0	3087	2691	6115	2123	3771

Table S7. *Projected national emissions of CO$_2$ by different energy sources for 2050 (thousands of tonnes C yr^{-1}) for the 2°C scenario.* Results from simulations in Ref[33]. Negative values indicate carbon removal by negative emissions technology.

Source	China	India	USA	Brazil	Indonesia	Canada	Mexico	France	Italy	Germany	Spain	Poland
1 Power own use & trans.	297226	72263	47554	-5175	19701	-713.494	17756	-2097	2243	33061	4494	-6829
2 O. energy own use & tr	105840	1824	10025	3947	2910	3929	5766	1737	1910	3119	1410	1118
3 Hydrogen production	0	0	0	0	0	0	0	0	0	0	0	0
4 Iron & steel	19891	14868	3882	5576	961	654	3066	1962	568	1342	151	186
5 Non-ferrous metals	4933	1033	2869	12004	47	134	9.6	80.5	83	35	126	257
6 Chemicals	35	2816	19384	6407	617	1171	2136	1903.6	291	0	403	2524
7 Non-metallics nes	188432	6605	21170	3461	1730	120	12814	2329	1846	57	2624	1493
8 Ore-extra.(non-energy)	18	871	0	3421	904	3728	522	171	76	173	41	30
9 Food, drink & tob.	118	246	13700	1712	461	0	228	1007	140	22	61	302
10 Tex., cloth. & footw.	191	924	1371	481	392	0	0	21.5	65	191	19	22
11 Paper & pulp	1.5	168	2312	3373	583	14.4	362	223	194	1.8	107	69
12 Engineering etc	77.6	448	1921	0	66.5	0	74	1225	897	185	776	551
13 Other industry	2177	0	268	3192	18133	1068	2964	279	229	201	1186	131
14 Construction	358	0	52	0	195	178	4.6	324	28	21	116	50
15 Rail transport	381	2133	56	723	0	1250	137	49	39	93	32	22
16 Road transport	24881	194905	37147	54054	2169	7066	10189	3990	9264	8797	6760	6194
17 Air transport	8139	11996	26363	5609	3410	3922	2423	1573	669	666	1251	60
18 Other transp. serv.	924	141	2039	1925	165	1826	0.001	757	711	357	540	0.4
19 Households	6104	92330	50821	3633	4482	5069	107	917	972	1135	201	2711
20 Agriculture, forestry	974	51906	292	9236	1253	299	699	1978	1537	473	1714	1155
21 Fishing	0	0	0	0	0	0	0	190	145	0	0	0.1
22 Other final use	1294	17241	37677	988	911	21.8	239	1756	2453	3303	77	681
23 Non-energy use	0	0	0	0	0	0	0	3208	2734	6515	2126	3807

Table S8. *Projected national electricity generation by different energy sources for 2050 (GWh yr^{-1}) for the business-as-usual (bau) scenario.* Results from simulations in Ref[33]. CCS, carbon capture and storage; CC, combined cycle; IGCC, integrated gasification CC; CCGT, CC gas turbine; BIGCC, biomass IGCC, PV, photovoltaic; CSP, concentrated solar power; CNG, compressed natural gas

Power source	China	India	USA	Brazil	Indonesia	Canada	Mexico	France	Italy	Germany	Spain	Poland
1 Nuclear	125160	77114	432248	18102	0	38779	7812	434313	0	5131	29348	0
2 Oil	11955	93308	42327	28541	54323	4841	71993	3118	17529	24533	17444	5538
3 Coal	10227320	3941654	2506522	76324	276494	80264	93416	5130	7253	9734	4021	4343
4 Coal + CCS	40171	19801	11989	310	1551	245	362	290	626	24928	190	21470
5 IGCC	173284	131612	162095	382	18775	303	6080	97	200	3674	96	416
6 IGCC + CCS	145337	102677	91382	315	10986	242	2681	978	6916	167158	602	51920
7 CCGT	88710	256829	1607133	23844	156321	2856	246915	6311	126187	254831	9251	11027
8 CCGT + CCS	1121	3015	8187	428	1104	38	835	454	17674	33863	426	3043
9 Solid Biomass	2.8	63	1004	1417	2.1	11	10	986	883	33141	4812	406
10 S Biomass CCS	1552	1430	564	387	3.0	14	3.5	429	384	6293	736	2155
11 BIGCC	1921	1874	1202	450	3.9	15	5.1	327	507	8695	697	379
12 BIGCC + CCS	1670	1645	1002	378	3.5	12	3.9	2608	6125	11533	743	15806
13 Biogas	0	141587	110230	1808	0	1337	23220	4786	10966	21771	1183	1873
14 Biogas + CCS	0	443	246.1	7	0	5.0	11.034	88	167	256	15	33
15 Tidal	10	0	0	0	0	7.8	0	318	0	0	0	0
16 Large Hydro	2665707	535008	406894	1003336	22350	564936	85883	171183	107326	82020	65882	19264
17 Onshore	55845	15246	979293	109463	3.7	238208	138314	13641	10459	48208	1933	4949
18 Offshore	732	1362	684	178	0.004	35	19	2178	304	1545	415	205
19 Solar PV	60935	64802	79157	0	49	119	3687	106391	80379	268704	194386	99714
20 CSP	3.6	0	246	0	0	0	0	0	0	0	3547	0
21 Geothermal	877	0	38957	0	28974	0	33436	0	12795	1604	0	0
22 Wave	0.16	0	0	0	0	0.01	0	21	0	0	0	0
23 Fuel Cells	0	0	24	0	0	0	0	17	3.2	1.7	0	0.002
24 CHP	0	0	10	0	0	0	0	0	2.7	1.7	3.9	0	0.018
TOTAL	13602314	5389470	6481396	1265670	570943.2	932267.8	714686.5	753666.7	406684.9	1007628	335727	242541

Table S9. *Projected national electricity generation by different energy sources for 2050 (GWh yr^{-1}) for the 2°C scenario.* Results from simulations in Ref[33]. CCS, carbon capture and storage; CC, combined cycle; IGCC, integrated gasification CC; CCGT, CC gas turbine; BIGCC, biomass IGCC, PV, photovoltaic; CSP, concentrated solar power; CNG, compressed natural gas

Power Source	China	India	USA	Brazil	Indonesia	Canada	Mexico	France	Italy	Germany	Spain	Poland
1 Nuclear	418781	166230	950479	33078	0	29626	23815	448225	0	10335	39875	0
2 Oil	19793	45544	18998	11272	15910	792	25227	2137	14097	14017	13696	2654
3 Coal	1362105	357516	140047	7126	6821	850	3792	5150	3331	17126	4976	258
4 Coal + CCS	166127	46799	18151	293	16038	51	740	202	540	8098	247	7938
5 IGCC	60936	7787	3322	58	158	6.3	52	104	82	4365	146	43
6 IGCC + CCS	1552557	268333	85500	272	50820	44	6553	504	3266	44142	688	42498
7 CCGT	1264876	437008	904446	10160	136005	175	123693	5594	78527	241824	15954	2075
8 CCGT + CCS	696260	190977	172568	1017	76197	27	62429	454	23097	23869	927	18559
9 Solid Biomass	300452	56115	12204	8566	131	106	92	1609	2133	26942	5395	1091
10 S Bio.+ CCS	75897	21519	9598	18259	400	1989	109	1453	944	6356	841	9716
11 BIGCC	66647	1657	11612	1219	39	14	114	502	1783	6646	772	2249
12 BIGCC + CCS	947314	264486	268057	18976	2960	1844	3403	13072	34621	10471	829	22985
13 Biogas	0	3695	93375	4454	0	1111	44831	7693	18597	31773	3184	3310
14 Biogas + CCS	0	4694	95260	103	0	261	171	3459	464	610	2960	3376
15 Tidal	22	0	0	0	0	5.7	0	394	0	0	0	0
16 Large Hydro	2454544	265623	680421	1168908	31638	491740	120922	151917	107478	61823	64878	17118
17 Onshore	595116	210065	1736840	192445	2357	176572	198160	16455	12218	62826	4820	11766
18 Offshore	37664	40476	32179	1568	35	35	1262	2133	867	4170	1055	13725
19 Solar PV	3760883	686159	136105	0	41745	380	3887	94725	74434	189110	197508	85561
20 CSP	609	0	859	0	0	0	0	0	0	0	4296	0
21 Geothermal	1818	0	48864	0	208366	0	42324	0	11833	1156	0	0
22 Wave	12	0	0	0	0	0.015	0	30	0	0	0	0
23 Fuel Cells	0	0	24	0	0	0	0	21	4.8	12	0	0
24 CHP	0	0	11	0	0	0	0	2.2	2.0	4.9	0	0.006
TOTAL	13782413	3074683	5418920	1477774	589620	705629	661576	755835.2	388318.8	765675.9	363047	244922

Table S10. *Summary of national rail logistical operations for 2050. Analysis assumes 3000 t payload.*

| Country | Origin-Destination (km) | | Full trip (km) | | Cost in US dollars | | $/KM | $/t/km | | | CO$_2$ Emissions | |
	Mean	StdD	Mean	StdD	Mean	StdD			Mean	StdD	kgCO$_2$/t/km	g/t/km
Brazil	53.0	104.5	106.1	209.1	875	1724.0	16.5	0.00550	2416.6	4763.0	0.0152	15.2
Canada	476.8	388.3	953.6	776.5	8187	6666.4	17.2	0.00572	21723.7	17689.2	0.0152	15.2
China	65.1	112.5	130.2	224.9	618	1066.7	9.5	0.00316	1622.5	2802.7	0.0083	8.3
France	178.1	156.6	356.2	313.1	2156	1895.0	12.1	0.00403	3246.0	2853.2	0.0061	6.1
Germany	180.7	162.3	361.4	324.7	1855	1666.9	10.3	0.00342	3292.7	2958.4	0.0061	6.1
India	207.4	201.0	414.7	402.0	4399	4264.1	21.2	0.00707	11336.5	10988.2	0.0182	18.2
Indonesia	44.0	72.9	88.0	145.7	591	978.6	13.4	0.00448	2004.3	3319.8	0.0152	15.2
Italy	210.5	154.9	421.0	309.7	2534	1863.9	12.0	0.00401	3836.4	2822.1	0.0061	6.1
Mexico	35.0	84.7	70.0	169.3	452	1093.9	12.9	0.00431	1594.7	3857.6	0.0152	15.2
Poland	506.4	258.3	1012.8	516.7	4717	2406.8	9.3	0.00311	9228.3	4708.1	0.0061	6.1
Spain	319.1	216.1	638.2	432.2	3211	2174.7	10.1	0.00335	5815.1	3938.1	0.0061	6.1
USA	473.2	438.7	946.4	877.3	5599	5190.1	11.8	0.00394	17247.7	15988.0	0.0121	12.1

Table S11. *Summary of national road logistical operations for 2050 in the business-as-usual scenario. Analysis assumes 40 t HGV electric payload.*

| Country | Cost in US dollars | | | | | CO_2 Emissions | | | | |
	Max	Mean	StdD	$/KM	$/t/km	Max	Mean	StdD	Kg CO_2/t/km	g/t/km
Brazil	439	42.1	51.0	0.23	0.00584	223	21.4	26.0	0.0030	2.97
Canada	319	80.8	59.4	0.14	0.00360	281	71.2	52.3	0.0032	3.17
China	213	25.2	23.6	0.15	0.00380	1486	176.2	164.9	0.0265	26.51
France	141	32.5	26.6	0.21	0.00520	9	2.0	1.7	0.0003	0.32
Germany	229	56.0	51.6	0.34	0.00840	151	37.1	34.1	0.0056	5.56
India	125	28.0	21.3	0.13	0.00320	1066	238.8	181.8	0.0273	27.27
Indonesia	240	22.8	51.2	0.12	0.00296	1959	186.7	418.6	0.0242	24.20
Italy	191	61.2	40.9	0.35	0.00864	133	42.6	28.5	0.0060	6.02
Mexico	292	35.2	56.7	0.27	0.00680	538	64.9	104.2	0.0125	12.55
Poland	238	114.3	56.5	0.23	0.00576	25	12.2	6.0	0.0006	0.61
Spain	209	66.5	44.8	0.23	0.00572	74	23.4	15.8	0.0020	2.01
USA	264	69.4	62.4	0.18	0.00456	1049	275.2	247.5	0.0181	18.09

Table S12. *Summary of national road logistical operations for 2050 in the 2°C scenario. Analysis assumes 40 t HGV electric payload.*

| Country | Cost in US dollars | | | | | CO_2 Emissions | | | | |
	Max	Mean	StdD	$/KM	$/ton/km	Max	Mean	StdD	$kgCO_2/t/km$	g/t/km
Brazil	439	42.0	51.0	0.233	0.0058	0	-3.68	4.49	-0.00051	-0.510
Canada	319	80.8	59.4	0.143	0.0036	0	-3.29	2.46	-0.00015	-0.146
China	213	25.2	23.6	0.151	0.0038	177	21.03	19.68	0.00316	3.165
France	141	32.5	26.5	0.207	0.0051	0	-2.53	2.11	-0.00041	-0.405
Germany	229	56.0	51.6	0.335	0.0083	172	42.25	38.91	0.00633	6.333
India	125	28.0	21.3	0.127	0.0032	134	30.05	22.87	0.00343	3.432
Indonesia	240	22.8	51.2	0.118	0.0029	397	37.81	84.77	0.00499	4.900
Italy	191	61.1	40.8	0.345	0.0086	19	6.00	4.02	0.00084	0.847
Mexico	292	35.2	56.6	0.272	0.0068	169	20.35	32.79	0.00393	3.932
Poland	238	114.3	56.4	0.230	0.0057	0	-81.11	40.07	-0.00409	-4.087
Spain	209	66.5	44.8	0.228	0.0057	66	21.07	14.21	0.00181	1.812
USA	264	69.3	62.40	0.182	0.0045	75	19.58	17.62	0.00128	1.287

Table S13. *Summary of mining component costs and relevant weights as used in our analysis.*
Mine Characteristics: 10,000 t ore/day, open-pit, 1:1 strip ratio, 365 days a year, located in USA, based on analyses in Ref[25] with additional data from Ref[26].

Capital Costs ($)		Labour Factor (wl)	Fuel Factor (wf)	Independent Factor (ws)
Equipment	13,956,400	0.0	0.0	1.0
Haul Roads/site work	2,183,300	0.1	0.7	0.2
Preproduction Shipping	824,200	0.0	0.0	1.0
Buildings	3,217,500	0.3	0.3	0.4
Electrical System	179,200	0.3	0.3	0.4
Working Capital	1,631,900	1.0	0.0	0.0
Engineering and Management	2,105,500	1.0	0.0	0.0
Contingency	2,246,600	0.0	0.0	1.0
Total Capital Costs ($)	**26,344,600**			
Total Capital Costs ($/t) (Assuming a 10 year mine lifespan, operating 365 days a year at 10,000 t day^{-1})	**0.72**			

Operating Costs ($/t ore)		Labour Factor (*wl*)	Fuel Factor (*wf*)	Independent Factor (*ws*)
Fuel	0.81	0.0	1.0	0.0
Supplies and Materials (excl. fuel)	0.88	0.0	0.0	1.0
Labor	1.91	1.0	0.0	0.0
Equipment Operation	1.44	0.0	0.8	0.2
Administration	0.69	1.0	0.0	0.0
Sundry Items	0.57	0.0	0.0	1.0
Total Operating Costs ($/t)	**6.30**			
Total Costs ($/t)	**7.02**			

Table S14. *Summary of global datasets, resolution and sources.* All gridded datasets were resampled to 1/6° resolution with the nearest neighbour method[37]. We minimized data gaps resulting from spatially overlaying grids, using image dilation from the Matlab Image Processing Toolbox[63]. This procedure morphologically expands the data boundaries of an image thus reducing the background/no-value pixels and achieving a better overlap between gridded data.

Variable	Resolution	Year	Reference
Crop net primary production	1/12°	2000	21,22
Soil pH (0-30 cm)	1/20°	2012	64
Soil temperature (0-5 cm)	1.25° × 1.875°	2050	65
Diesel Price	Country Level	2010-2017	66
Gross National Income per Capita	Country Level	2010-2017	67
Industrial electricity tariffs	Country Level	Various	68-70
Mining Costs	Country Level	2010-2017	25,26
Crop evapotranspiration	1/12°	1998-2002	11
Crop irrigation	1/2°	1998-2002	10
Precipitation	1/24°	1998-2002	9
GDP projections for SSPs	-	2000-2100	40

Table S15. *Chemical data from a column leach experiment on construction and demolition waste compared with typical water quality standard ranges.* Even without separating out cement waste from other materials[59], very little of the leachate contained elemental concentrations above typical water quality standard ranges[60-62]. The exceptions are Sb and Se. However, these are less concentrated in the unmixed cement waste[59].

C&D leached element[48]	Mean	Typical Range for Water Quality Standards[60-61]
Aluminium (mg l^{-1})	1.6	0.2
Calcium (mg l^{-1})	395	250
Iron (mg l^{-1})	0.085	0.2 to 1
Potassium (mg l^{-1})	125	10 to 12
Sodium (mg l^{-1})	90	170 to 200
Magnesium (mg l^{-1})	0.0485	50
S as sulphate (mg l^{-1})	75	250 to 400
Arsenic (µg l^{-1})	16	10 to 50
Barium (µg l^{-1})	800	700 to 1000
Cadmium (µg l^{-1})	1	2.5 to 5
Chloride (µg l^{-1})	55000	250000
Cobalt (µg l^{-1})	9.5	3 to 100 (ref[60])
Chromium (µg l^{-1})	55	5 to 250
Copper (µg l^{-1})	50	1 to 2000
Lithium (µg l^{-1})	190	700 (Ref[61])
Manganese (µg l^{-1})	6	50 to 500
Molybdenum (µg l^{-1})	15	70
Nickel (µg l^{-1})	35.5	20 to 200
Phosphorous (µg l^{-1})	60	400 to 5000
Lead (µg l^{-1})	9.5	4 to 250
Antimony (µg l^{-1})	36	5
Selenium (µg l^{-1})	32	10
Vanadium (µg l^{-1})	18.5	20 to 100
Zinc (µg l^{-1})	130	8 to 5000

4. Supplementary references

1. Berner, R.A. Rate control of mineral dissolution under earth surface conditions. *Am. J. Sci.* **278,** 1235–1252 (1978).
2. Maher, K. The dependence of chemical weathering rates on fluid residence time. *Earth Plan. Sci. Lett.* **294,** 101-110 (2010).
3. Navarre-Sitchler, A. & Brantley, S. Basalt weathering across scales. *Earth Plan Sci. Lett.* **261,** 321-334 (2007).
4. Nelson, P.N. & Su, N. Soil pH buffering capacity: a descriptive function and its application to some acidic tropical soils. *Aust. J. Soil Sci.* **48,** 201-207 (2010).
5. Cerling, T. Carbon dioxide in the atmosphere: evidence from Cenozoic and Mesozoic paleosols. *Am. J. Sci.*, **291**, 377–400 (1991).
6. Taylor, L., Banwart, S.A., Leake, J.R. & Beerling, D.J. Modelling the evolutionary rise of ectomycorrhizal on sub-surface weathering environments and the geochemical carbon cycle. *Am. J. Sci.*, **311**, 369–403 (1991).
7. Banwart, S.A., Berg, A. & Beerling, D.J. Process-based modelling of silicate mineral weathering responses to increasing atmospheric CO_2 and climate change. *Biogeochem. Cycles*, **23,** GB4013.
8. Taylor, L.L. *et al.* Enhanced weathering strategies for stabilizing climate and averting ocean acidification. *Nat. Clim. Change* **6**, 402–406 (2016).
9. Abatzoglou, J.T., Dobrowski, S.Z., Parks, S.A. & Hegewisch, K.C. TerraClimate, a high-resolution global dataset of monthly climate and climatic water balance from 1958-2015. *Sci. Data,* **5,** 170191 (2018).
10. Huang, Z.W. *et al.* Reconstruction of global gridded monthly sectoral water withdrawals for 1971-2010 and analysis of their spatiotemporal patterns. *Hydrol. Earth Syst. Sci.* **22,** 2117-2133 (2018).
11. Siebert, S. & Doll, P. Quantifying blue and green virtual water contents in global crop production as well as potential production losses without irrigation. *J. Hydrol.* **384,** 198-217 (2010).
12. Aagaard, P. & Helgeson, H. C. Thermodynamic and kinetic constraints on reaction-rates among minerals and aqueous-solutions. 1. Theoretical considerations. *Am J Sci* **282**, 237-285, (1982).
13. Lasaga, A. C. Chemical-kinetics of water-rock iInteractions. *J. Geophys. Res.* **89**, 4009-4025 (1984).
14. Brantley, S.L., Kubicki, J.D. & White, A.F. *Kinetics of water-rock interaction* (Springer, New York, 2008).
15. Brantley, S. L. & Mellott, N.P. Surface area and porosity of primary silicate minerals. *Am Mineral* **85**, 1767-1783 (2000).
16. Petavratzi, E., Kingman, S. & Lowndes, I. Particulates from mining operations: A review of sources, effects and regulations. *Miner Eng* **18**, 1183-1199, doi:10.1016/j.mineng.2005.06.017 (2005).
17. Renforth, P. The potential of enhanced weathering in the UK. *Int J Greenh Gas Con* **10**, 229-243, doi:10.1016/j.ijggc.2012.06.011 (2012).
18. Cepuritis, R., Garboczi, E. J., Ferraris, C. F., Jacobsen, S. & Sorensen, B. E. Measurement of particle size distribution and specific surface area for crushed concrete aggregate fines. *Adv Powder Technol* **28**, 706-720, doi:10.1016/j.apt.2016.11.018 (2017).
19. Harley, A.D. & Gilkes, R.J. Factors influencing the release of plant nutrient elements from silicate rock powders: a geochemical overview. *Nutr. Cycl. Agroecosys.* **56,** 11-36 (2000).
20. Taylor, L.L. *et al.* Biological evolution and the long-term carbon cycle: integrating mycorrhizal evolution and function into the current paradigm. *Geobiology*, **7,** 171-191 (2009).
21. Ramankutty, N., Evan, A. T., Monfreda, C. & Foley, J. A. Farming the planet: 1. Geographic distribution of global agricultural lands in the year 2000. *Global Biogeochem. Cycles* **22**, doi:Artn Gb100310.1029/2007gb002952 (2008).
22. Monfreda, C., Ramankutty, N. & Foley, J. A. Farming the planet: 2. Geographic distribution of crop areas, yields, physiological types, and net primary production in the year 2000. *Global Biogeochem. Cycles* **22**, doi:Artn Gb102210.1029/2007gb002947 (2008).
23. Renforth, P. & Henderson, G. Assessing ocean alkalinity for carbon sequestration. *Rev. Geophys.* **55**, 636–674 (2017)

24. Salisbury, J.E. *et al.* Seasonal observations of surface waters in two Gulf of Maine estuary-plume systems: Relationships between watershed attributes, optical measurements and surface pCO_2. *Estuarine, Coast. Shelf Sci.* **77,** 245–252 (2008).

25. Darling, P. & Society for Mining Metallurgy and Exploration (U.S.). *SME mining engineering handbook*. 3rd edn (Society for Mining, Metallurgy, and Exploration, 2011).

26. InfoMine. *InfoMine, Mining Cost Service*, http://www.infomine.com/ (2009).

27. Hartmann, J. & Moosdorf, N. The new global lithological map database GLiM: A representation of rock properties at the Earth surface. *Geochem Geophy Geosy* **13**, doi:Artn Q1200410.1029/2012gc004370 (2012).

28. UNEP-WCMC and IUCN (2018), *Protected Planet: The World Database on Protected Areas (WDPA)/The Global Database on Protected Areas Management Effectiveness (GD-PAME)]* (Cambridge, UK: UNEP-WCMC and IUCN 2018).

29. ROTARU, A. S. *et al.* Modelling a Logistic Problem by Creating an Origin-Destination Cost Matrix using GIS Technology. *Bulletin UASVM Horticulture*, **71,** (2014).

30. Osorio, C. Dynamic origin-destination matrix calibration for large-scale network simulators. *Transportation Research Part C: Emerging Technologies* **98**, 186-206 (2019).

31. International Energy Agency. *The Future of Rail, Opportunities for energy and the environment* (International Energy Agency, Paris, France, 2019).

32. Liimatainen, H., van Vliet, O. & Aplyn, D. The potential of electric trucks – an international commodity-level analysis. *App. Energy*. 236, 804-814 (2019).

33. Mercure, J.-F. *et al.* Macroeconomic impact of stranded fossil fuel assets. *Nat. Clim. Change* **8,** 588-593 (2018).

34. Global Petrol Prices, data collection and methods. 2019. Available from: https://www.globalpetrolprices.com/data/.

35. Moosdorf, N., Renforth, P. & Hartmann, J. Carbon dioxide efficiency of terrestrial enhanced weathering. *Env. Sci. Technol.* **48,** 4809-4816 (2014).

36. Tromans, D. Mineral comminution: energy efficiency considerations. *Min. Engin.* **21,** 613-620 (2008).

37. Audet, C. & Dennis, J.E. Analysis of generalized pattern searches. *Siam. J Optimiz* .**13**, 889-903, doi:Pii S1052623400378742Doi 10.1137/S1052623400378742 (2003).

38. van Ruijven, B. J. *et al.* Long-term model-based projections of energy use and CO_2 emissions from the global steel and cement industries. *Resour. Conserv. Recycl.* **112,** 15–36 (2016).

39. The World Bank. *GDP (current US$)*, https://data.worldbank.org/indicator/NY.GDP.MKTP.CD (2016).

40. Bauer, N. *et al.* Shared socio-economic pathways of the energy sector – quantifying the narratives. *Glob. Environ. Change* **42,** 316-330 (2017).
(available at https://tntcat.iiasa.ac.at/SspDb)

41. Xi, F. *et al.* Substantial global carbon uptake by cement carbonation. *Nat. Geosci.* **9,** 880-883 (2016).

42. U.S. Geological Survey. *Mineral Commodity Summaries 2006*. (US Geological Survey, Washington, USA, 2006).

43. Parkhurst, D.L. & Appelo, C.A.J. *Description of input and examples for PHREEQC version 3: a computer program for speciation, batch-reaction, one-dimensional transport, and inverse geochemical calculations*. (U.S. Geological Survey Techniques and Methods, 497 pp., 2013).

44. Cavigelli, M.A., Deming, S.R. Probyn, L.K. & Harwood, R.R. *Michigan Field Crop Ecology: Managing Biological Processes for Productivity and Environmental Quality* (Michigan State University Extension Bulletin E-2646, East Lansing, Michigan, USA., 1989).

45. Pohlmann, M. *et al.* Pore water chemistry reveals gradients in mineral transformation across a model basaltic hillslope. *Geochem. Geophys. Geosys.* **17,** 2054-2069 (2016).

46. Akter, M. & Akagi, T. Effect of fine root contact on plant-induced weathering of basalt. *Soil Sci Plant Nutr* **51**, 861-871, doi:DOI 10.1111/j.1747-0765.2005.tb00121.x (2005).

47. Akter, M. & Akagi, T. Dependence of plant-induced weathering of basalt and andesite on nutrient conditions. *Geochem J* **44**, 137-150, doi:DOI 10.2343/geochemj.1.0052 (2010).

48. Quirk, J. *et al.* Evolution of trees and mycorrhizal fungi intensifies silicate mineral weathering. *Biol. Letts.* **8,** 1006-10011 (2012).

49. Quirk, J. *et al.* Ectomycorrhizal fungi and past high CO_2 atmospheres enhance mineral weathering through increased below-ground carbon-energy fluxes. *Biol. Letts.* **10,** 20140375 (2014).

50. Gislason, S.R. & Oelkers, E.H. Mechanism, rates and consequences of basaltic glass dissolution: II. An experimental study of the dissolution rates of basaltic glass as a function of pH and temperature. *Geochim. et Cosmochim. Acta*, **67,** 3817-3832 (2003).

51. Silverman, B.W. *Density Estimation for Statistics and Data Analysis* (Chapman & Hall, London, 1986).

52. Palandri, J. L. & Kharaka, Y. K. A Compilation of Rate Parameters of Water-Mineral Interaction Kinetics for Application to Geochemical Modeling. Report No. Open File Report 2004-1068, (U.S. Geological Survey, California, USA, 2004).

53. Kopittke, P.M. & Blamey, F.P.C. Theoretical and experimental assessment of nutrient solution composition in short-term studies of aluminium rhizotoxicity. *Plant Soil*, **406,** 311–326 (2016).

54. Wuenscher, R. *et al.* A comparison of 14 soil phosphorus extraction methods applied to 50 agricultural soils from Central Europe. *Plant Soil Environ.***61,** 86-96 (2015).

55. Torrent, J., DelCampillo, M.C. & Barron, V. Predicting cation exchange capacity from hygroscopic moisture in agricultural soils of Western Europe. *Span. J. Agri. Res.* **13,** e11SC01, 3 pages.

56. Russell, A.E., Laird, D. & Mallarino, A.P. Nitrogen fertilization and cropping system impacts on soil quality in Midwestern mollisols. *Soil Sci. Soc. Am. J.* **70,** 249–255 (2006).

57. Baquy M.A., Li, J-Y., Shi, R., J.Kamran, M.A. & Ku, R-K. Higher cation exchange capacity determined lower critical soil pH and higher Al concentration for soybean. *Environ. Sci. Poll. Res.*, **25,** 6980–6989 (2018).

58. Dau, Y., Qiao, X. & Wang, X. Study on cation exchange capacity of agricultural soils. IOP Conf. Series: Materials Science and Engineering, **392,** 042039 (2018).

59. Butera, S., Christensen, T.H. & Astrup, T.F. Composition and leaching of construction and demolition waste: Inorganic elements and organic compounds. *J. Hazardous Mat.* **276,** 302-311 (2014).

60. Esdat Environmental Database Management Software. www.esdat.net http://esdat.net/Environmental%20Standards/UK/Landfill%20Directive%20Appendix%208%20Selected%20Water%20Quality%20Standards.pdf

61. Scottish Environment Protection Agency. *Environmental Quality Standards and Standards for Discharges to Surface Waters.* Supporting Guidance (WAT-SG-53) (SEPA, 2019).

62. Water Research Center. Lithium in Drinking Water and Brine Water Marcellus Shale Citizen Private Well Monitoring. https://water-research.net/index.php/lithium

63. MATLAB 2017b, Image Processing Toolbox, The MathWorks, Inc., Natick, Massachusetts, United States

64. Wieder, W.R., J. Boehnert, G.B. Bonan, and M. Langseth. 2014. Regridded Harmonized World Soil Database v1.2. Data set. Available on-line [http://daac.ornl.gov] from Oak Ridge National Laboratory Distributed Active Archive Center, Oak Ridge, Tennessee, USA.

65. Taylor, K. E., Stouffer, R. J. & Meehl, G. A. An Overview of CMIP5 and the Experiment Design. *B Am Meteorol Soc* **93**, 485-498, doi:10.1175/Bams-D-11-00094.1 (2012).

66. The World Bank. *Pump price for diesel fuel (US$ per liter)* https://data.worldbank.org/indicator/EP.PMP.DESL.CD (2017).

67. The World Bank. *Gross National Income per Capita*, https://data.worldbank.org/indicator/ny.gnp.pcap.pp.cd (2017).

68. BEIS. *Department for Business, Energy & Industrial Strategy: Industrial Electricity Prices in the IEA*, <https://www.gov.uk/government/statistical-data-sets/international-industrial-energy-prices> (2017).

69. ANEEL. *Brazilian Electricity Regulatory Agency*, <http://www.aneel.gov.br/> (2018)
70. AC. Russian Energy - 2015. (Analytical Centre For the Goverment Of The Russian Federation, 2016).